Comparative Study of the Hydrostatic and Non-hydrostatic Versions of the MOHID Model in Performance Benchmarking for Tsunami Events

João Pedro Carrilho da Silva

Thesis to obtain the Master of Science Degree in

Civil Engineering

Supervisors: Prof. António Alberto Pires Silva

Doctor Paulo Miguel Chambel Filipe Lopes Leitão

Examination Committee

Chairperson: Prof. António Alexandre Trigo Teixeira

Supervisor: Doctor Paulo Miguel Chambel Filipe Lopes Leitão

Members of the committee: Prof. Ramiro Joaquim de Jesus Neves

Prof. António Bento Franco

September 2016

DEDICATÓRIA

Este trabalho é dedicado à minha mãe e irmã pelo apoio e palavras de encorajamento constantes, ao meu pai por ser a maior força influenciadora no meu percurso académico e cujos conselhos e opiniões considero inestimáveis (ainda que nunca me ouvirá admitir tal coisa), e à Joana que esteve ao meu lado nos últimos 5 anos e sem a qual, possivelmente, ainda vagueraria pelos corredores do Técnico.

AKNOWLEDGEMENTS

First, I would like to thank both my supervisors, Prof. António Pires Silva and Dr. Paulo Chambel Leitão, for all the support and guidance they provided along the development of this dissertation. Without their passion and scientific rigor, this work, as it stands, wouldn’t have been possible.

I would also like to thank Hidromod, which was my home for 5 months and provided the necessary resources to run all the numerical model simulations. On that note, I must also thank KORDI for kindly accepting the request for the data regarding the Tohoku earthquake and tsunami.

Last but not least, I would like to thank dr. João Tiago Ribeiro for his help in the development of the Sendai Plain inundation maps.

RESUMO

A tragédia que sucedeu o tsunami do oceano Índico em 2004 foi uma força impulsionadora para o desenvolvimento de medidas de mitigação por parte de países com extensas zonas costeiras. Tradicionalmente o planeamento destas medidas é feito com o auxílio de modelos numéricos hidrostáticos, como os baseados nas equações não lineares para águas pouco profundas. No entanto, novos estudos sugerem que a evolução e espraiamento de tsunamis pode ser fortemente influenciado pela dispersão associada a efeitos não hidrostáticos, podendo resultar em valores até 60% superiores de espraiamento na zona costeira do que os calculados pelos referidos modelos hidrostáticos. Foi na sequência destes factos que o seguinte trabalho foi desenvolvido.

Esta dissertação consiste na apresentação e validação de uma versão não hidrostática do modelo MOHID, que recentemente introduziu um novo método de correção de pressão. Adicionalmente, também foi estudada como a versão não hidrostática do MOHID se compara em relação à versão hidrostática de modo a determinar as possíveis vantagens do novo modelo.

O processo de validação foi inspirado na metodologia de benchmarking para modelos numéricos, e orientada ao estudo de tsunamis, proposta pela organização americana National Oceanic and Atmospheric Administration. O processo de validação consistiu numa bateria de testes com complexidade de geometria crescentes, com o objectivo de comparar os resultados numéricos com as sias soluções analíticas, resultados laboratoriais e dados de campo. Estes resultados incluem instantes da propagação da onda, séries temporais da elevação da superfície livre e mapas de inundação.

Palavras chave: Tsunami, MOHID, modelo numérico, não hidrostático, NOAA.

ABSTRACT

The tragedy that followed the Boxing Day tsunami of 2004 was a driving force in the development of mitigation measures by countries with large coastal areas. Traditionally, the planning of these measures was done with the aid of hydrostatic numerical models, such as the ones based on the non-linear shallow water equations. However, recent studies suggest that the evolution and run-up of tsunamis can be strongly influenced by dispersion due to non-hydrostatic effects, which can result in up to 60% higher values of coastal run-up than the ones calculated by the aforementioned hydrostatic models. It was in light of these facts that the following work was developed.

This dissertation consists in the presentation and validation of a non-hydrostatic version of the MOHID model, which features a newly introduced pressure correction method. Furthermore, in order to determine which advantages the new model might have over its hydrostatic counterpart, it was also studied how both models compare against each other.

The validation process was inspired by the benchmarking methodology proposed by the United States' National Oceanic and Atmospheric Administration, for numerical models aimed at the study of tsunami events. It consisted in running a battery of tests, with increasingly complex geometries, with the objective of comparing the numerical results with their analytical solutions, laboratory data or field data. These results include snapshots of the wave propagation, time series of surface elevations and inundation maps.

Keywords: Tsunami, MOHID, numerical model, non-hydrostatic, NOAA.

CONTENTS

TABLE OF FIGURES

NOTATION

Roman letters

Symbol	Description	Units (S.I.)
A	Area of the computational cell	m^2
$FluxI$	Flow flux in I direction	m^3s^{-1}
g	Earth gravity	$m\ s^{-2}$
H	Total water depth $(h+\eta)$	m
h	Water depth measured from the average water level	m
j,k,l	Vector index	(-)
k	Turbulent kinetic energy by mass unit	$m^2\ s^{-2}$
n	Manning's roughness coefficient	$m^{-1/3}\ s^{-1}$
p	Pressure	$N\ m^{-2}$
p_a	Atmospheric pressure	$N\ m^{-2}$
q	Normalized non-hydrostatic pressure	m
Re	Reynolds number	(-)
R_{ij}	Reynold's stress tensor	$N\ m^{-2}$
t	Time	s
U,V,W	Depth averaged velocities in the x, y and z directions, respectively	$m\ s^{-1}$
u,v,w	Velocities in the x, y and z directions, respectively	$m\ s^{-1}$
$\bar{u}$	Time averaged velocity	$m\ s^{-1}$
u'	Random component of velocity (in a turbulent flow)	$m\ s^{-1}$
u_i	Velocity component in the i direction	$m\ s^{-1}$
x,y,z	Position vector components	m
x_i	i position vector component	m

Greek letters

Symbol	Description	Units (S.I.)
δ_{ij}	Kronecker symbol	(-)
Δt	Time interval	s
η	Free surface elevation	m
v	Kinematic viscosity	$m^2\ s^{-2}$
v_t	Eddy, or turbulent, viscosity	$m^2\ s^{-2}$
ρ	Fluid specific mass	$Kg\ m^{-3}$
ρ_0	Reference fluid specific mass	$Kg\ m^{-3}$
τ_{ij}	Stress tensor	$N\ m^{-2}$

1. INTRODUCTION

1.1. MOTIVATION AND OBJECTIVES

Tsunami is a Japanese word that originated from the composition of the words "*tsu*" (harbour) and "*nami*" (wave), and can be literally translated as harbour wave. The term was supposedly coined by Japanese fishermen that returned to their villages to find them devastated by water when they hadn't noticed anything out of the ordinary while in the open sea. This led them to believe that the huge wave responsible for the disaster had originated inside the harbour.

Tsunamis occur mainly due to sudden changes in the configuration of the sea bed in the sequence of which results a great shift of water mass. This kind of phenomena is usually associated with certain types of earthquakes but there can also be other causes. These other causes can either be natural like volcanic eruptions, underwater landslides or asteroid impacts, or man-made like underwater explosions.

The aforementioned shift in the water column produces on the surface of the sea long period waves (between 10 minutes and 2 hours) with big wavelengths that can reach hundreds of kilometres. In the ocean these waves can travel with velocities of over 900 km/h with an amplitude of only a few centimetres. For this reason they usually go unnoticed by boats and aerial monitoring systems. Near the shore the waves feel bottom which results in a decrease of velocity and shoaling. In these conditions waves can reach heights of over 30 m (National Oceanic and Atmospheric Administration, 2015).

The Sumatra earthquake followed by the Boxing Day tsunami, as it would later be known, happened on the cost of Indonesia on 26 December 2004. Due to this event the life of over 225 000 people was lost in countries around the Indian ocean, particularly in Indonesia, Sri Lanka, Thailand and India. This catastrophe strengthened the interest in the development of plans to mitigate the possible effects of future tsunamis in countries or regions that are susceptible to this kind of phenomena (Synolakis & Bernard, 2006).

The concerns that arose from the Boxing Day tsunami are also shared by Portugal which has also been hit by a devastating earthquake followed by tsunami on 1 November 1755 known as the Great Lisbon earthquake. It was in this light that the interest and opportunity for this dissertation emerged.

The company Hidromod, lda., which directly supported the development of this dissertation, was tasked by the Portuguese civil protection agency (Autoridade Nacional de Proteção Civil) to delimit inundation areas of several regions of the Portuguese coast in case of a tsunami event.

Traditionally this kind of studies have been mainly developed with the aid of hydrostatic models such as COMCOT, MOHID, TUNAMI-N2 and COMMIT/MOST, see Baptista *et al.* (2008); Fernandes (2009); Gardi *et al.* (2011); Hyun *et al.* (2013). In this type of models the vertical accelerations are neglected and the hydrostatic approximation is applied to the vertical momentum equation (see chapter 2.4.1.). This is a valid approximation when the wavelength of the disturbance is much larger than the height of the water column, which often holds true for the case of tsunamis generated by sub-marine earthquakes.

However, studies following the Boxing Day tsunami, such as Horrillo *et al.* (2006); Kulikov (2006) and Walters (2005), suggest the evolution and run-up of tsunamis can be strongly influenced by dispersion due to non-hydrostatic effects. This can result in up to 60% higher values of coastal run-up than the ones calculated by models based on the non-linear shallow water equations (NSWE), for example.

For the aforementioned reasons combined with the active development of three dimensional non-hydrostatic models in recent years, such as Casulli & Stelling (1998); Casulli & Zanolli (2002) and Cui, Pietrzak, & Stelling (2012), it was decided that this was a good opportunity to evaluate the added value of introducing non-hydrostatic capabilities in the MOHID modelling system..

Theias (2005) was the first to introduce a non-hydrostatic approach in MOHID following a method proposed by Casulli & Zanolli (2002). However, this method assumes a hydrostatic approach for the surface layer, which may result in an important limitation in some situations. To overcome this, a Keller-box approach was proposed by Stelling (Stelling & Zijlema, 2003) (Cui et al. 2012) in order to compute the non-hydrostatic pressure correction applied to a single layer (2D flow). This method showed to be very promising and was included in MOHID by Leitão (Leitão, 2016).

To determine whether the non-hydrostatic version of MOHID is ready for field hindcast and forecast it’s necessary to undergo a process of validation, which is the first objective of this dissertation. The second objective is the comparison of the model results with the ones produced by its hydrostatic counterpart as a way to determine what kind of benefits non-hydrostatic models bring to the table.

1.2. METHODOLOGY

The validation process of the non-hydrostatic model was based on a benchmarking methodology proposed by North American organization NOAA (National Oceanic and Atmospheric Administration) designed for wave propagation models and applied to the simulation of tsunamis. The methodology is detailed in Synolakis *et al.* (2007).

All the laboratory results and data used for setting up the tests in the numerical models can be found in NOAA’s centre for tsunami research website at *http://nctr.pmel.noaa.gov/benchmark/* .

The validation process is divided in three separate test categories: comparison of a set of results with their respective analytical solutions, reproduction of laboratory experiments and reproduction of real tsunami events.

The bathymetries used in the numerical models were, for the most part, created based on the available descriptions of the laboratory experiments. For the test cases with more complex geometries, namely the Monai Valley experiment and Tohoku tsunami, the resources were found online in NOAA’s centre for tsunami research website for the first case and requested to the Korean Ocean Research and Development Institute (KORDI) for the second.

The forcing conditions in the numerical models for all the presented test cases, except for the Tohoku tsunami and Monai Valley experiment, was done inside the boundaries of the computational grid. The initial conditions of the solitary waves, namely elevation and velocity, were calculated using their respective equations presented in either Archambeau *et al.* (1999) or Staroszczyk (2011), depending on which profile fitted better the measured solutions and whether higher order equations were necessary to ensure the model’s stability. The generation of the studied waves for all remaining test cases will be presented in their respective chapters.

Each test case was ran in both the hydrostatic and non-hydrostatic versions of MOHID and the obtained results were compared with their respective analytic solution or recorded data (depending on the type of test) and are presented along with the spatial and time steps used in their simulations.

The analysed results, produced by the numerical models, include snapshots of certain simulation instants, time series generated for certain spatial locations and inundation maps created using MOHID GIS.

1.3. OUTLINE OF THE DISSERTATION

The present dissertation is divided in four main chapters and references.

In Chapter 2 are presented the main equations of motion used by MOHID. A special focus is given to the pressure correction method introduced in the current non-hydrostatic version of MOHID along with its numerical formulation.

The results obtained in the benchmarking tests for both the hydrostatic and non-hydrostatic versions of the model are described in Chapter 3. A commentary of the results is presented for each test case.

The main conclusions of this dissertation along with recommendations for future studies are included in Chapter 4.

2. EQUATIONS OF MOTION

2.1. REYNOLDS-AVERAGED NAVIER-STOKES EQUATIONS

2.1.1. NAVIER-STOKES EQUATIONS

The Navier-Stokes equations are a generalization of the equations of motion first published by Leonhard Euler in 1759 for incompressible and inviscid fluids. In 1821 Claude-Louis Navier introduced the concept of viscosity into the equations in order to describe the flow of viscous fluids. In 1845 George Gabriel Stokes improved the equations proposed by Navier making it possible to obtain exact solutions for some particular cases of flows.

The Navier-Stokes equations can be written in tensor notation as seen in (2.2) for a Newtonian fluid. In this type of fluids the shear stress is linearly proportional to the velocity gradient in the direction perpendicular to the plane of shear (White, 2005). In these conditions the stress tensor can be written as:

$$\tau_{ij} = -p\delta_{ij} + v\rho\left(\frac{\partial u_i}{\partial x_j} + \frac{\partial u_j}{\partial x_i}\right) \tag{2.1}$$

where *p* is pressure, u_i is the velocity component in the *i* direction, x_i is the *i* position vector component, v is the kinematic viscosity and ρ is the fluid specific mass.

$$\frac{\partial u_j}{\partial t} + u_i\frac{\partial u_j}{\partial x_i} = \frac{1}{\rho}\frac{\partial \tau_{ij}}{\partial x_j} + g_j \tag{2.2}$$

The system of equations (2.2) can be simplified, as shown in (2.5), and completed using the continuity equation (2.4) thus forming a closed system. This continuity equation is a particular form of the mass conservation equation (2.3) for incompressible fluids (dρ/dt=0).

$$\frac{\partial \rho}{\partial t} + \frac{\partial \rho u_i}{\partial x_i} = \frac{\partial \rho}{\partial t} + u_i\frac{\partial \rho}{\partial x_i} + \rho\frac{\partial u_i}{\partial x_i} = \frac{d\rho}{dt} + \rho\frac{\partial u_i}{\partial x_i} = 0 \tag{2.3}$$

$$\frac{\partial u_i}{\partial x_i} = 0 \tag{2.4}$$

$$\frac{\partial u_j}{\partial t} + u_i\frac{\partial u_j}{\partial x_i} = -\frac{1}{\rho}\frac{\partial p}{\partial x_j} + v\frac{\partial^2 u_j}{\partial {x_i}^2} + g_j \tag{2.5}$$

2.1.2. AVERAGE EQUATIONS

Turbulent flows are particularly complex to analyse due to their apparently chaotic nature. However even amidst all the chaos we can find a little semblance of order. Putting aside the lyrical description of the problem and by observing a turbulent flow it's possible to identify certain regular patterns as it is illustrated in Figure 2.1, made by Leonardo da Vinci in his own study of turbulent flows. It's from this simple concept of pattern identification that originated the mathematical technique known as Reynolds decomposition, named after its creator Osbourne Reynolds.

Figure 2.1 – Sketch of a turbulent flow by Leonardo da Vinci circa 1500.

The Reynold's decomposition consists in the separation of the average and fluctuating parts of a quantity. Applying this concept to the instantaneous velocity field we get (2.6)

$$u(x,y,z,t) = \overline{u(x,y,z,t)} + u'(x,y,z,t) \tag{2.6}$$

where the time average operator is given by (2.7).

$$\bar{u} = \frac{1}{\mathrm{T}} \int_0^{\mathrm{T}} u(t+\tau)\, d\tau \tag{2.7}$$

As a consequence, the following properties of the time average operator, represented in (2.8) and (2.9), are held.

$$\overline{u'} = 0 \tag{2.8}$$

$$\bar{\bar{u}} = \bar{u} \tag{2.9}$$

When the operator (2.7) is applied to (2.5) the Reynolds-averaged Navier-Stokes (RANS) equations are obtained. These equations are represented in (2.10).

$$\frac{\partial \bar{u}_j}{\partial t}+\bar{u}_i\frac{\partial \bar{u}_j}{\partial x_i}=-\frac{1}{\rho}\frac{\partial \bar{p}}{\partial x_j}+\frac{\partial}{\partial x_i}\left(v\frac{\partial \bar{u}_j}{\partial x_i}-\overline{u'_i u'_j}\right)+g_j \tag{2.10}$$

2.2. TURBULENCE MODELLING

From the decomposition process described previously arises the problem of closing the system of equations (2.10) since the term $\overline{u'_i u'_j}$ is unkown. This term is linked to the turbulent nature of the flow and is called the Reynolds stress tensor (R_{ij}).

In order to close the equation system the effects of the Reynolds stresses must be modelled (Chen & Jaw, 1998).

2.2.1. EDDY VISCOSITY MODELS

The concept of eddy viscosity (or Boussinesq hypothesis for turbulence modelling) was first introduced in 1887 by Joseph Boussinesq in order to solve the closing problem of the set of equations (2.10). This hypothesis consists in modelling the Reynold's stress tensor by analogy to the expression presented in (2.1) since they generate similar effects in the flow. Therefore this tensor will be proportional to the mean velocity gradient (Chen & Jaw, 1998) and an eddy or turbulent viscosity coefficient, written as v_t, is introduced.

By introducing this coefficient we can write the Reynold's stress tensor as seen in (2.11)

$$\overline{u'_i u'_j}=\frac{2}{3}k\delta_{ij}-v_t\left(\frac{\partial \bar{u}_i}{\partial x_j}+\frac{\partial \bar{u}_j}{\partial x_i}\right) \tag{2.11}$$

where k, represented in (2.12), is the kinetic turbulent energy per unit mass.

$$k=\frac{1}{2}\overline{u'_i u'_i} \tag{2.12}$$

Replacing (2.11) in (2.10) solves the closing problem. The RANS equations hereby assume the form presented in (2.13). All turbulence models based in this type of parameterization are generically called eddy viscosity models.

$$\frac{\partial \bar{u}_j}{\partial t}+\bar{u}_i\frac{\partial \bar{u}_j}{\partial x_i}=-\frac{1}{\rho}\frac{\partial \bar{p}}{\partial x_j}+(v+v_t)\frac{\partial^2 \bar{u}_j}{\partial {x_i}^2}+g_j \tag{2.13}$$

For the sake of convenience, it's possible to rewrite (2.13) using v_h and v_v as the horizontal and vertical components, respectively, of the effective viscosity $(v+v_t)$ therefore obtaining equations

(2.14) and (2.15) while the continuity equation can be written as seen in (2.16). For these equations *i* and *j* take the values of 1 and 2 only.

$$\frac{\partial \bar{u}_j}{\partial t} + \bar{u}_i \frac{\partial \bar{u}_j}{\partial x_i} = -\frac{1}{\rho}\frac{\partial \bar{p}}{\partial x_j} + v_h \frac{\partial^2 \bar{u}_j}{\partial {x_j}^2} + v_v \frac{\partial^2 \bar{u}_j}{\partial z^2} \tag{2.14}$$

$$\frac{\partial \bar{w}}{\partial t} + \bar{u}_i \frac{\partial \bar{w}}{\partial x_i} + \bar{w}\frac{\partial \bar{w}}{\partial z} = -\frac{1}{\rho}\frac{\partial \bar{p}}{\partial z} + v_h \frac{\partial^2 \bar{w}}{\partial {x_j}^2} + v_v \frac{\partial^2 \bar{w}}{\partial z^2} + g \tag{2.15}$$

$$\frac{\partial \bar{u}_i}{\partial x_i} + \frac{\partial \bar{w}}{\partial z} = 0 \tag{2.16}$$

In order to close the problem of turbulence modelling it's still needed to assign a value to the eddy viscosity coefficient. In the case of the tests performed later in this dissertation this was done either by assigning a static value, when it was sensible to do so, or by using a Smagorinsky model (Smagorinsky, 1963).

2.3. AVERAGED MASS CONSERVATION EQUATION

Since only mean flow values will be used from here on out, the mean operator will be dropped for the sake of simplicity.

2.3.1. BOUSSINESQ APPROXIMATION

A traditional simplification used in coastal hydrodynamic modelling is the Boussinesq approximation. By using this approximation fluid density differences are ignored except when they appear in terms multiplied by g (gravity acceleration) (Tritton, 1977). The relative homogeneity of the ocean in its horizontal dimension, when compared to the variation of certain characteristics with depth, like density and temperature, makes this a reasonable approximation.

When the Boussinesq approximation is applied to (2.15) the result is

$$\frac{\partial w}{\partial t} + \bar{u}_i \frac{\partial w}{\partial x_i} + \bar{w}\frac{\partial w}{\partial z} = -\frac{1}{\rho}\frac{\partial p}{\partial z} + v_h \frac{\partial^2 w}{\partial {x_j}^2} + v_v \frac{\partial^2 w}{\partial z^2} + \frac{\rho}{\rho_0} g \tag{2.17}$$

where ρ_0 is a reference fluid specific mass.

2.3.2. FREE SURFACE ELEVATION

The free surface elevation is measured relative to a reference level, usually the mean sea level, as illustrated in Figure 2.2.

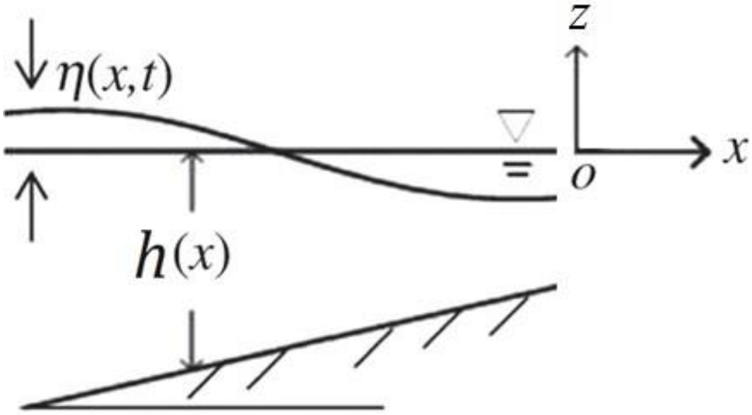

Figure 2.2 – Definition of the free surface elevation. Adapted from (Chen, Li, Hsu, & Ng, 2012).

By integrating the continuity equation (2.16) in the vertical direction (z) while adopting the kinematic boundary conditions (2.18) and (2.19) for the free surface ($z = \eta$) and bottom ($z = -h$), respectively, the equation (2.20) for the free surface behaviour can be obtained (Theias, 2005).

$$w|_{z=\eta} = \frac{\partial \eta}{\partial t} + u_j \frac{\partial \eta}{\partial x_j} \tag{2.18}$$

$$w|_{z=-h} = -u_j \frac{\partial h}{\partial x_j} \tag{2.19}$$

$$\frac{\partial \eta}{\partial t} + \frac{\partial}{\partial x}\left(\int_{-h}^{\eta} u\, dz\right) + \frac{\partial}{\partial y}\left(\int_{-h}^{\eta} v\ dz\right) = \frac{\partial \eta}{\partial t} + \frac{\partial (HU)}{\partial x} + \frac{\partial (HV)}{\partial y} = 0 \tag{2.20}$$

In equation (2.20), H is total water depth $(h + \eta)$. U and V are depth averaged velocities and are defined as shown in (2.21) and (2.22).

$$U = \frac{1}{H}\int_{-h}^{\eta} u\ dz \tag{2.21}$$

$$V = \frac{1}{H}\int_{-h}^{\eta} v\ dz \tag{2.22}$$

2.4. NON-HYDROSTATIC MODEL

2.4.1. GOVERNING EQUATIONS

The momentum balance equation (2.17) can be written as follows in the vertical direction:

$$\frac{\partial w}{\partial t} + u\frac{\partial w}{\partial x} + v\frac{\partial w}{\partial y} + w\frac{\partial w}{\partial z} = -\frac{1}{\rho_0}\frac{\partial p}{\partial z} + v_h\left(\frac{\partial^2 u_j}{\partial x^2} + \frac{\partial^2 u_j}{\partial y^2}\right) + v_v\frac{\partial^2 w}{\partial z^2} + \frac{\rho}{\rho_0}g \tag{2.23}$$

The hydrostatic version of MOHID assumes that the vertical acceleration terms as well as the vertical components of the friction forces in (2.23) are small when compared to pressure and gravitational forces and, therefore, can be dropped (hydrostatic approximation), resulting in equation (2.24).

$$0 = -\frac{\partial p}{\partial z} + \rho g \tag{2.24}$$

The inclusion of non-hydrostatic effects in the model is done by decomposing the pressure term presented in (2.24) in its hydrostatic components and adding the normalized non-hydrostatic pressure term, q, as shown in equation (2.25) taken from (Theias, 2005). Assuming $q = 0$ is the equivalent of considering a system with hydrostatic pressure.

$$\begin{aligned} &\frac{1}{\rho_0}p(x,y,z,t) \\ &= \underbrace{\frac{1}{\rho_0}p_a(x,y,t)}_{Atmospheric} + \underbrace{\underbrace{g\int_{-h}^{\eta}\frac{\rho-\rho_0}{\rho_0}\,dz}_{Baroclinic} + \underbrace{g[\eta(x,y,t)-z]}_{Barotropic}}_{Hydrostatic} + \underbrace{q(x,y,z,t)}_{Non-hydrostatic} \\ &= p'(x,y,z,t) + q(q,x,y,z,t) \end{aligned} \tag{2.25}$$

By replacing (2.25) in (2.17), the system (2.26) is obtained.

$$\frac{\partial u_j}{\partial t} + u_i\frac{\partial u_j}{\partial x_i} = -\frac{1}{\rho_0}\frac{\partial p'}{\partial x_j} - \frac{\partial q}{\partial x_j} + v_h\left(\frac{\partial^2 u_j}{\partial x^2} + \frac{\partial^2 u_j}{\partial y^2}\right) + v_v\frac{\partial^2 u_j}{\partial z^2} + \frac{\rho}{\rho_0}g \tag{2.26}$$

Applying (2.26) and integrating over depth with the kinematic boundary conditions (2.18) and (2.19), results in momentum equations (2.27) and (2.28) for directions x and y respectively (Cui *et al.* 2012).

$$\frac{\partial U}{\partial t} + U\frac{\partial U}{\partial x} + V\frac{\partial U}{\partial y} + g\frac{\partial \eta}{\partial x} + \frac{1}{H}\int_{-h}^{\eta}\frac{\partial q}{\partial x}dz + \frac{gn^2}{H^{4/3}}U\sqrt{U^2+V^2} = 0 \tag{2.27}$$

$$\frac{\partial V}{\partial t} + U\frac{\partial V}{\partial x} + V\frac{\partial V}{\partial y} + g\frac{\partial \eta}{\partial y} + \frac{1}{H}\int_{-h}^{\eta}\frac{\partial q}{\partial y}dz + \frac{gn^2}{H^{4/3}}V\sqrt{U^2+V^2} = 0 \tag{2.28}$$

In the equations presented n is Manning's roughness coefficient and the friction forces are parameterized with an empirical formulation – The Manning expression.

Using Leibniz's rule to integrate the non-hydrostatic pressure gradient, and considering that the non-hydrostatic pressure at the free surface is zero ($q|_{z=\eta} = 0$), results in:

$$\int_{-h}^{\eta} \frac{\partial q}{\partial x} dz = \frac{\partial}{\partial x}\int_{-h}^{\eta} q dz - q|_{z=\eta}\frac{\partial \eta}{\partial x} + q|_{z=-h}\frac{\partial(-h)}{\partial x} = \frac{\partial}{\partial x}\int_{-h}^{\eta} q\, dz - q|_{z=-h}\frac{\partial h}{\partial x} \qquad (2.29)$$

Studies show that the following approximation to the integral (trapezoidal rule)

$$\int_{-h}^{\eta} q dz = \frac{Hq|_{z=-h}}{2} \qquad (2.30)$$

gives the best dispersion relation (Cui *et al.* 2012), which replaced in (2.29) results in (2.31). Since the non-hydrostatic pressure at the free surface is zero ($q|_{z=\eta} = 0$), for the sake of simplicity q is read as the non-hydrostatic pressure at the bottom, from this point forward, and the subscript is dropped.

$$\int_{-h}^{\eta} \frac{\partial q}{\partial x} dz = \frac{1}{2}H\frac{\partial q}{\partial x} + \frac{q}{2}\frac{\partial(\eta - h)}{\partial x} \qquad (2.31)$$

Inserting (2.31) into momentum equations (2.27) and (2.28) results in equations (2.32) and (2.33).

$$\frac{\partial U}{\partial t} + U\frac{\partial U}{\partial x} + V\frac{\partial U}{\partial y} + g\frac{\partial \eta}{\partial x} + \frac{1}{2}\frac{\partial q}{\partial x} + \frac{1}{2}\frac{q}{H}\frac{\partial(\eta - h)}{\partial x} + \frac{gn^2}{H^{4/3}}U\sqrt{U^2 + V^2} = 0 \qquad (2.32)$$

$$\frac{\partial V}{\partial t} + U\frac{\partial V}{\partial x} + V\frac{\partial V}{\partial y} + g\frac{\partial \eta}{\partial y} + \frac{1}{2}\frac{\partial q}{\partial y} + \frac{1}{2}\frac{q}{H}\frac{\partial(\eta - h)}{\partial y} + \frac{gn^2}{H^{4/3}}V\sqrt{U^2 + V^2} = 0 \qquad (2.33)$$

The vertical momentum equation, presented below, also needs to be considered. This equation can be deduced by replacing (2.25) in (2.23) (Theias, 2005).

$$\frac{\partial w}{\partial t} + u\frac{\partial w}{\partial x} + v\frac{\partial w}{\partial y} + w\frac{\partial w}{\partial z} = -\frac{\partial q}{\partial z} + v_h\left(\frac{\partial^2 w}{\partial x^2} + \frac{\partial^2 w}{\partial y^2}\right) + v_v\frac{\partial^2 w}{\partial z^2} \qquad (2.34)$$

Since the advective and dissipative terms are small when compared with the non-hydrostatic pressure term they can be omitted (Cui *et al.* 2012), resulting in equation (2.35).

$$\frac{\partial w}{\partial t} = -\frac{\partial q}{\partial z} \qquad (2.35)$$

The vertical momentum equation based upon the Keller-box scheme, and a linear approximation for the vertical dependency of the vertical velocity w, presented in (Stelling & Zijlema, 2003), becomes (Cui *et al.* 2012):

$$\frac{\partial w}{\partial t} = \frac{\partial}{\partial t}\left(\frac{w_\eta + w_{-h}}{2}\right) = -\left(\left.\frac{\partial q}{\partial z}\right|_{z=\eta} + \left.\frac{\partial q}{\partial z}\right|_{z=-h}\right)/2 = \frac{q}{H} \tag{2.36}$$

Equation (2.36) can be written in a discretized form as:

$$\frac{w_\eta^{n+1} - w_\eta^n + w_{-h}^{n+1} - w_{-h}^n}{2\Delta t} = \frac{q^{n+1}}{H} \tag{2.37}$$

Equations (2.20), (2.32), (2.33) and (2.36) together with continuity equation (2.16), form the governing equations for depth-integrated, non-hydrostatic free-surface flows (Cui *et al.* 2012).

Since the term for non-hydrostatic pressure q is not the real non-hydrostatic pressure at the bottom, but rather just a numerical parameter used to resolve the dispersion, in order to construct the vertical profile for non-hydrostatic pressure $q(z)$, the following requirements must be fulfilled (Cui *et al.* 2012):

$$q(z)|_{z=\eta} = 0 \tag{2.38}$$

$$\int_{z=-h}^{z=\eta} q(z) = \frac{1}{2}Hq \tag{2.39}$$

$$\left.\frac{\partial q(z)}{\partial z}\right|_{z=\eta} = -2\frac{q}{H} \tag{2.40}$$

$$\left.\frac{\partial q(z)}{\partial z}\right|_{z=-h} = 0 \tag{2.41}$$

Equation (2.42) is one of the functions that meets all requirements presented above.

$$q(z) = \frac{2q}{3}\left[1 - \left(\frac{z+h}{H}\right)^3\right] \tag{2.42}$$

2.4.2. NUMERICAL FORMULATION

The governing equations are solved using the pressure projection method presented in Stelling & Zijlema (2003) which was first introduced by Chorin (1968).

In the first step of this method the momentum equations are solved without the non-hydrostatic pressure terms. This yields an approximate velocity field, denoted as $\tilde{U}^{n+1}$ and $\tilde{V}^{n+1}$, which might be not divergence free and thus incompatible with an incompressible flow. This velocity field is then used as an input for the second step, in which the horizontal and vertical velocities are corrected by the non-hydrostatic pressures and substituted into the continuity equation (2.16). This results in Poisson equations for the dynamic pressure q. Once the system with unknowns of

q is solved the horizontal and vertical velocities are updated with the values of q. The new water levels are then computed using the free surface elevation equation (2.20) (Cui *et al.* 2012).

The details of the first step of the method are described in Martins *et al.* (2001). The velocity solution for the second step is presented below.

$$U^{n+1} = \tilde{U}^{n+1} - \Delta t \left[\frac{1}{2} \frac{\partial q^{n+1}}{\partial x} + \frac{1}{2} \frac{\partial q^{n+1}}{H^n} \left(\frac{\partial \eta^n}{\partial x} - \frac{\partial h}{\partial x} \right) \right] \tag{2.43}$$

$$V^{n+1} = \tilde{V}^{n+1} - \Delta t \left[\frac{1}{2} \frac{\partial q^{n+1}}{\partial y} + \frac{1}{2} \frac{\partial q^{n+1}}{H^n} \left(\frac{\partial \eta^n}{\partial y} - \frac{\partial h}{\partial y} \right) \right] \tag{2.44}$$

In the present model it's assumed that there is no vertical velocity at the bottom. Since the advective and dissipative terms were dropped in the vertical momentum equation, in the second step, the approximation of the vertical velocity $\widetilde{w}^{n+1}$ is the same as the solution from the previous step (i.e. $\widetilde{w}^{n+1} = w^n$). The vertical velocity can be expressed by the non-hydrostatic pressure by using equation (2.45) (Cui *et al.* 2012).

$$w_\eta^{n+1} = \widetilde{w}_\eta^{n+1} + 2\Delta t \frac{q^{n+1}}{H} \tag{2.45}$$

2.4.3. MOHID IMPLEMENTATION

The numerical formulation, synthetized in equations (2.43), (2.44) and (2.45), was added to the MOHID hydrodynamic module considering a second step where the hydrostatic solution ($\tilde{n}^{n+1}, \tilde{U}^{n+1}, \tilde{V}^{n+1}, \widetilde{FluxX}^{n+1}, \widetilde{FluxY}^{n+1}$, where *Flux* represents the product of the computational cell area by the velocity of the flow) is corrected. In a first step the non-hydrostatic pressure correction *q* is computed using a semi-implicit scheme (ADI[1]). In a second step the horizontal velocity and fluxes using equations (2.43) and (2.44) are corrected. Finally, with the new fluxes by flow divergence, the sea level is also corrected and the vertical velocity of the sea level is updated using equation (2.45).

The process described above is translated into MOHID using the following numerical discretization:

For the pressure correction a field of *q* is computed for each *z* cell, combining equations (2.43), (2.44) and (2.45), and assuming a null divergence condition. The new pressure correction, q^{n+1}, is obtained for each cell (*i,j*) using the ADI approach. Through this method the non-hydrostatic correction is done alternated in each horizontal direction, as is represented in equations (2.46)

---

[1] The alternating direction implicit method (ADI) is a finite difference method for solving partial differential equations in which the values of the computational cells are implicitly solved alternately in the x and y directions for each iteration.

and (2.48) for the first time step in the *x* direction, and equations (2.47) and (2.49) for the second time step in the *y* direction. In these equations, A is the area of the computational cell.

$$U^{n+1}_{i,j-\frac{1}{2}}\,A^{n}_{i,j-\frac{1}{2}} - U^{n+1}_{i,j+\frac{1}{2}}\,A^{n}_{i,j+\frac{1}{2}} + \tilde{V}^{n+1}_{i-\frac{1}{2}j}\,A^{n}_{i-\frac{1}{2},j} - \tilde{V}^{n+1}_{i+\frac{1}{2},j}\,A^{n}_{i+\frac{1}{2},j} + w^{n+1}_{i,j,\eta}\,\Delta x_{i,j}\,\Delta y_{i,j} = 0 \tag{2.46}$$

$$\tilde{U}^{n+1}_{i,j-\frac{1}{2}}\,A^{n}_{i,j-\frac{1}{2}} - \tilde{U}^{n+1}_{i,j+\frac{1}{2}}\,A^{n}_{i,j+\frac{1}{2}} + V^{n+1}_{i-\frac{1}{2}j}\,A^{n}_{i-\frac{1}{2},j} - V^{n+1}_{i+\frac{1}{2},j}\,A^{n}_{i+\frac{1}{2},j} + w^{n+1}_{i,j,\eta}\,\Delta x_{i,j}\,\Delta y_{i,j} = 0 \tag{2.47}$$

$$\begin{gathered}\widetilde{FluxX}^{n+1}_{i,j-1/2} - \Delta t\left[\frac{1}{2}\left(\frac{q^{n+1}_{i,j}-q^{n+1}_{i,j-1}}{\Delta x}\right) + \frac{1}{2}\frac{\left(q^{n+1}_{i,j}+q^{n+1}_{i,j-1}\right)}{2H^{n}}\left(\frac{\partial\eta^{n}}{\partial x}-\frac{\partial h}{\partial x}\right)\right]A^{n}_{i,j-\frac{1}{2}} - \\ \widetilde{FluxX}^{n+1}_{i,j+\frac{1}{2}} + \Delta t\left[\frac{1}{2}\left(\frac{q^{n+1}_{i,j+1}-q^{n+1}_{i,j}}{\Delta x}\right) + \frac{1}{2}\frac{\left(q^{n+1}_{i,j+1}+q^{n+1}_{i,j}\right)}{2H^{n}}\left(\frac{\partial\eta^{n}}{\partial x}-\frac{\partial h}{\partial x}\right)\right]A^{n}_{i,j+\frac{1}{2}} + \\ \widetilde{FluxY}^{n+1}_{i-1/2,j} - \widetilde{FluxY}^{n+1}_{i+1/2,j} + \left(w^{n}_{i,j,\eta} + 2\Delta t\,\frac{q^{n+1}_{i,j}}{H^{n}}\right)\Delta x_{i,j}\Delta y_{i,j} = 0\end{gathered} \tag{2.48}$$

$$\begin{gathered}\widetilde{FluxY}^{n+1}_{i-\frac{1}{2},j} - \mathit{\Delta} t\left[\frac{1}{2}\left(\frac{q^{n+1}_{i,j}-q^{n+1}_{i-1,j}}{\mathit{\Delta} y}\right) + \frac{1}{2}\frac{\left(q^{n+1}_{i,j}+q^{n+1}_{i-1,j}\right)}{2H^{n}}\left(\frac{\partial\eta^{n}}{\partial y}-\frac{\partial h}{\partial y}\right)\right]A^{n}_{i-\frac{1}{2},j} - \widetilde{FluxY}^{n+1}_{i+\frac{1}{2},j} + \\ \mathit{\Delta} t\left[\frac{1}{2}\left(\frac{q^{n+1}_{i+1,j}-q^{n+1}_{i,j}}{\mathit{\Delta} y}\right) + \frac{1}{2}\frac{\left(q^{n+1}_{i+1,j}+q^{n+1}_{i,j}\right)}{2H^{n}}\left(\frac{\partial\eta^{n}}{\partial y}-\frac{\partial h}{\partial y}\right)\right]A^{n}_{i+\frac{1}{2},j} + \widetilde{FluxX}^{n+1}_{i,j-\frac{1}{2}} - \\ \widetilde{FluxX}^{n+1}_{i,j+\frac{1}{2}} + \left(w^{n}_{i,j,\eta} + 2\mathit{\Delta} t\,\frac{q^{n+1}_{i,j}}{H^{n}}\right)\mathit{\Delta} x_{i,j}\,\mathit{\Delta} y_{i,j} = 0\end{gathered} \tag{2.49}$$

The ADI approach generates for each time step a tridiagonal linear equation system. This system is given by expression (2.50) for the first time step (non-hydrostatic correction only in the *x* direction) and expression (2.51) for the second time step. In these expressions *D*, *E* and *F* represent, respectively, the lower, central and upper diagonals of the tridiagonal matrix algorithm used in the ADI method and *Ti* represents the independent term.

$$D_{i,j-1}\cdot q^{n+1}_{i,j-1} + E_{i,j}\cdot q^{n+1}_{i,j} + F_{i,j-1}\cdot q^{n+1}_{i,j+1} = Ti \tag{2.50}$$

$$D_{i-1,j}\cdot q^{n+1}_{i-1,j} + E_{i,j}\cdot q^{n+1}_{i,j} + F_{i-1,j}\cdot q^{n+1}_{i+1,j} = Ti \tag{2.51}$$

With the new pressure correction the horizontal water fluxes are corrected using equations (2.52) and (2.53) for the first and second time steps, respectively.

$$\begin{gathered}FluxX^{n+1}_{i,j-\frac{1}{2}} = \\ \widetilde{FluxX}^{n+1}_{i,j-\frac{1}{2}} - \Delta t\left[\frac{1}{2}\left(\frac{q^{n+1}_{i,j}-q^{n+1}_{i,j-1}}{\Delta x}\right) + \frac{1}{2}\frac{\left(q^{n+1}_{i,j}+q^{n+1}_{i,j-1}\right)}{2H^{n}}\left(\frac{\partial\eta^{n}}{\partial x}-\frac{\partial h}{\partial x}\right)\right]A^{n}_{i,j-\frac{1}{2}}\end{gathered} \tag{2.52}$$

$$FluxY_{i-\frac{1}{2},j}^{n+1} = \widetilde{FluxY}_{i-\frac{1}{2},j}^{n+1} - \Delta t\left[\frac{1}{2}\left(\frac{q_{i,j}^{n+1}-q_{i-1,j}^{n+1}}{\Delta \mathrm{y}}\right) + \frac{1}{2}\frac{\left(q_{i,j}^{n+1}+q_{i-1,j}^{n+1}\right)}{2H^n}\left(\frac{\partial\eta^n}{\partial y} - \frac{\partial h}{\partial y}\right)\right] A_{i-\frac{1}{2},j}^{n} \tag{2.53}$$

Next, the sea level is updated by computing the fluxes correction divergence as shown in equations (2.54) and (2.55) for the first and second time steps, respectively.

$$n_{i,j}^{n+1} = \tilde{\eta}_{i,j}^{n+1} + \frac{\Delta t}{\Delta x_{i,j}\cdot\Delta y_{i,j}}.\Bigg[\bigg[-\frac{1}{2}\left(\frac{q_{i,j}^{n+1}-q_{i,j-1}^{n+1}}{\Delta x}\right) + \frac{1}{2}\frac{\left(q_{i,j}^{n+1}+q_{i,j-1}^{n+1}\right)}{2H^n}\left(\frac{\partial\eta^n}{\partial x} - \frac{\partial h}{\partial x}\right)\bigg] A_{i,j-\frac{1}{2}}^{n} + \left[\frac{1}{2}\left(\frac{q_{i,j+1}^{n+1}-q_{i,j}^{n+1}}{\Delta x}\right) + \frac{1}{2}\frac{\left(q_{i,j+1}^{n+1}+q_{i,j}^{n+1}\right)}{2H^n}\left(\frac{\partial\eta^n}{\partial x} - \frac{\partial h}{\partial x}\right)\right]\cdot A_{i,j+\frac{1}{2}}^{n}\Bigg] \tag{2.54}$$

$$\eta_{i,j}^{n+1} = \tilde{\eta}_{i,j}^{n+1} + \frac{\Delta t}{\Delta x_{i,j}\cdot\Delta y_{i,j}}.\Bigg[-\bigg[\frac{1}{2}\left(\frac{q_{i,j}^{n+1}-q_{i-1,j}^{n+1}}{\Delta \mathrm{y}}\right) + \frac{1}{2}\frac{\left(q_{i,j}^{n+1}+q_{i-1,j}^{n+1}\right)}{2H^n}\left(\frac{\partial\eta^n}{\partial y} - \frac{\partial h}{\partial y}\right)\bigg] A_{i-\frac{1}{2},j}^{n} + \left[\frac{1}{2}\left(\frac{q_{i+1,j}^{n+1}-q_{i,j}^{n+1}}{\Delta \mathrm{y}}\right) + \frac{1}{2}\frac{\left(q_{i+1,j}^{n+1}+q_{i,j}^{n+1}\right)}{2H^n}\left(\frac{\partial\eta^n}{\partial y} - \frac{\partial h}{\partial y}\right)\right]\cdot A_{i+\frac{1}{2},j}^{n}\Bigg] \tag{2.55}$$

Finally, the vertical velocity in the surface is update using equation (2.56) in the end of each time step.

$${w_{i,j}}_{\eta}^{n+1} = {w_{i,j}}_{\eta}^{n} + 2\Delta t\frac{{q_{i,j}}^{n+1}}{H^n} \tag{2.56}$$

3. MODEL VALIDATION AND RESULTS ANALYSIS

3.1. ANALYTICAL BENCHMARKING

The comparison of the results produced by the model with analytical solutions is particularly useful in the validation of the discretization of the differential equations and approximations used by the model. However, analytical solutions are limited relatively simple examples that correspond to simplified form of those equations (Silva, 1991).

In this battery of tests, solitary waves of varying relative amplitude (A/h) were propagated along a constant depth channel. In order to keep a graphical consistency of the results, the wave amplitude was kept constant (2 m) and the water depth was changed between tests.

The numerical simulations results for relative amplitudes of 0.1, 0.125, 0.25 and 0.5 are presented from Figure 3.1 to Figure 3.4. As can be seen below, the non-hydrostatic model manages to maintain the phase, amplitude and the shape of the analytical solution for all tested cases except for a relative amplitude of 0.5, where both a little lag and loss of amplitude are noticeable. In opposition, the hydrostatic model fails to reproduce both the amplitude and shape of the analytical solution.

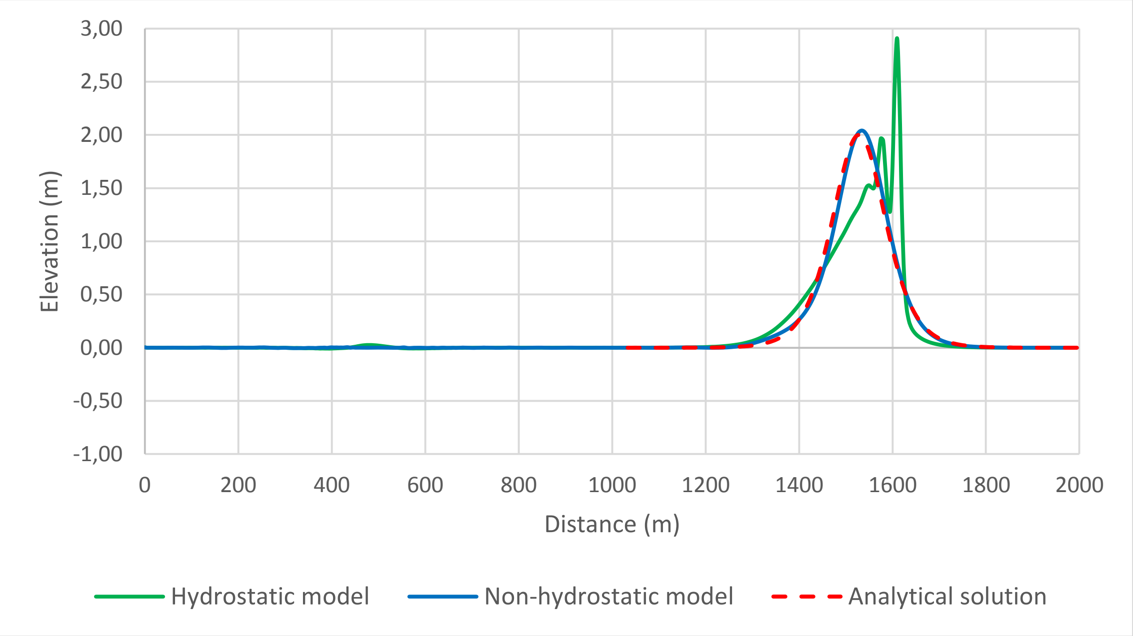

Figure 3.1 – Propagation of a solitary wave on a flat bottom channel, with both the hydrostatic and non-hydrostatic models, and comparison with the analytical solution. A/h=0.1; spatial step=5m; time step=0.05s.

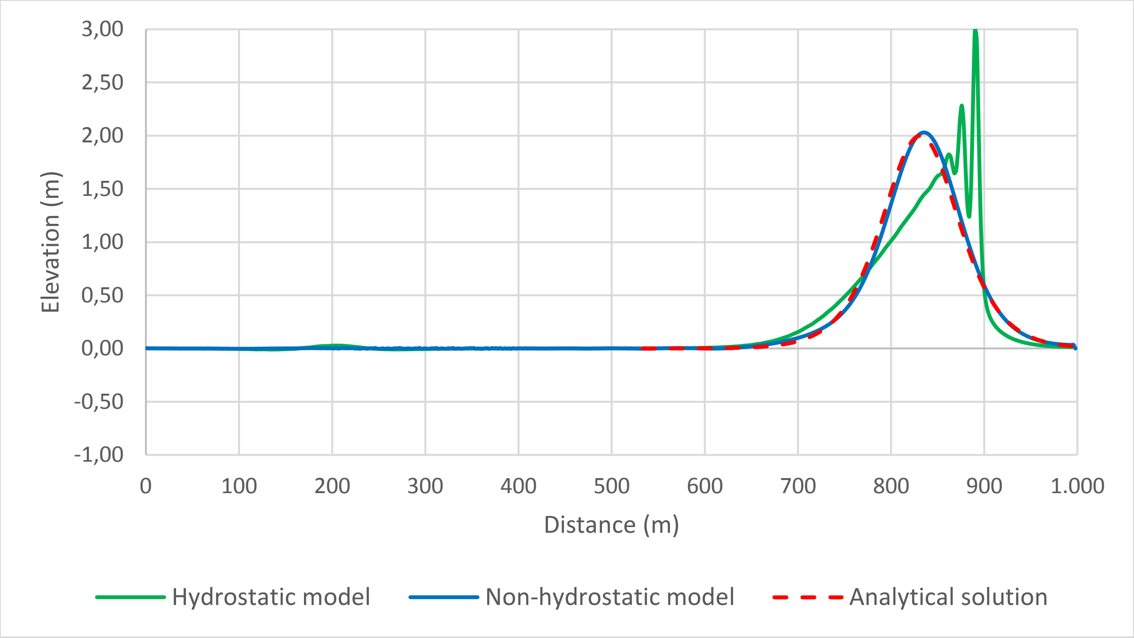

Figure 3.2 – Propagation of a solitary wave on a flat bottom channel, with both the hydrostatic and non-hydrostatic models, and comparison with the analytical solution. A/h=0.125; spatial step=2 m; time step=0.05 s.

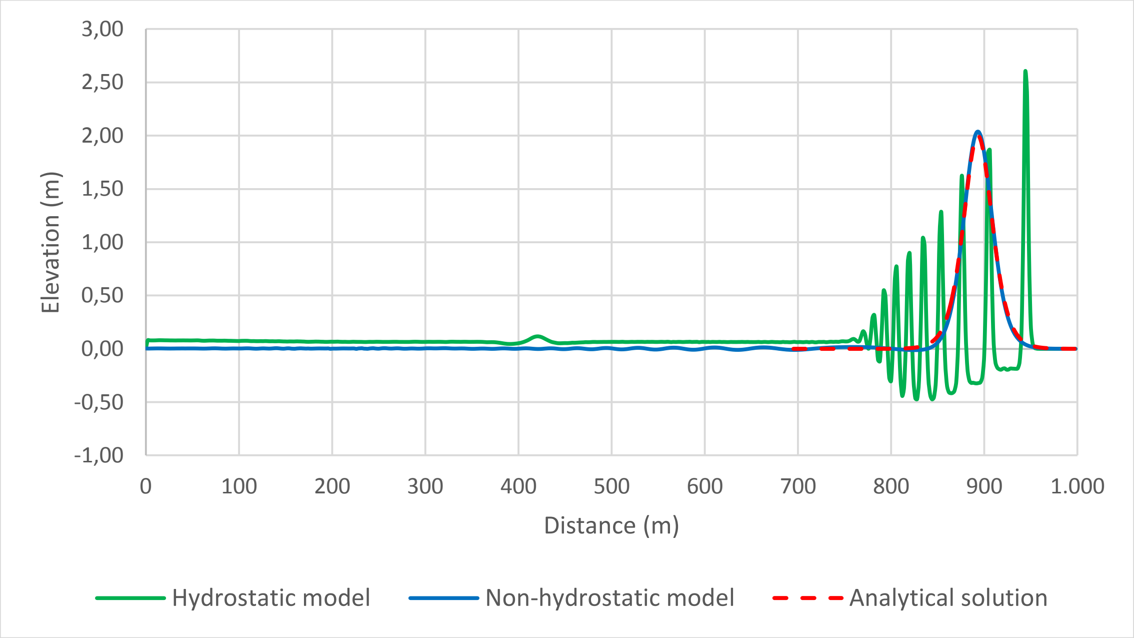

Figure 3.3 – Propagation of a solitary wave on a flat bottom channel, with both the hydrostatic and non-hydrostatic models, and comparison with the analytical solution. A/h=0.25; spatial step=2 m; time step=0.05 s.

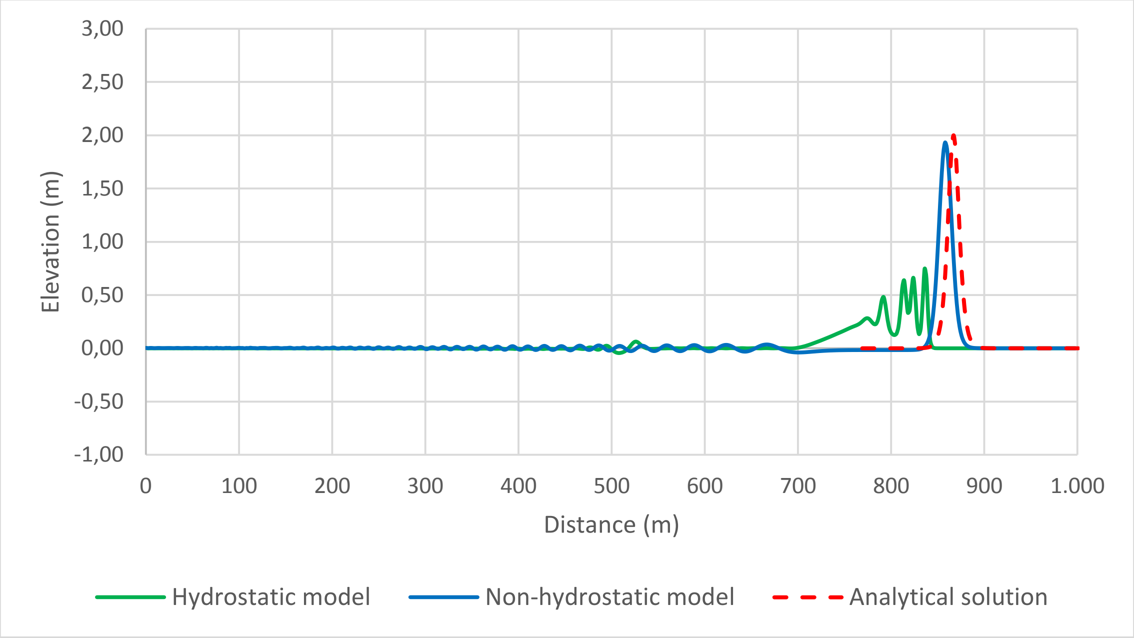

Figure 3.4 – Propagation of a solitary wave on a flat bottom channel, with both the hydrostatic and non-hydrostatic models, and comparison with the analytical solution. A/h=0.5; spatial step=2 m; time step=0.01s.

3.2. LABORATORY BENCHMARKING

The use of small scale physical models has been historically prevalent both to make predictions about maritime phenomena, that would later be scaled to prototypes, and, in more recent decades, to confirm and validate results produced by numerical models. Experience shows that numerical models that are able to closely reproduce results obtained in small scale laboratory experiments are also able to satisfactorily model tsunamis at a geophysical scale (Synolakis *et al.* 2007).

In order to guarantee the numerical model's stability in some of the test cases presented in the following chapters, it was necessary to scale up the bathymetries used in the numerical model in relation to the laboratory models. This is a valid procedure since, for the purpose of validating inundation models, the scale differences are not believed to be important (Synolakis *et al.* 2007). The same kind of procedure was also done in the benchmarking of FUNWAVE-TVD (a fully non-linear Boussinesq model) in Shi *et al.* (2012) and other numerical models ([NTHMP] National Tsunami Hazard Mitigation Program, 2012). However, a parameterization of roughness and viscous effects was required since these phenomena don't scale based on Froude number similitude.

3.2.1. SOLITARY WAVE ON A SIMPLE BEACH

The objective of this set of tests is to reproduce the laboratory results obtained for the propagation of a solitary wave on a constant depth channel adjoining a sloping beach.

The wave tank used in the laboratory tests is 31.73 m long, 60.96 cm deep and 39.97 cm wide and it's located at the California Institute of Technology in Pasadena, California. The bottom of the tank consists of stainless steel plates and the slope has a constant value of 1:19.85 (V:H). A more detailed description of the tank can be found in Synolakis (1986) and Synolakis (1987). A schematic representation of the test case is presented in Figure 3.5.

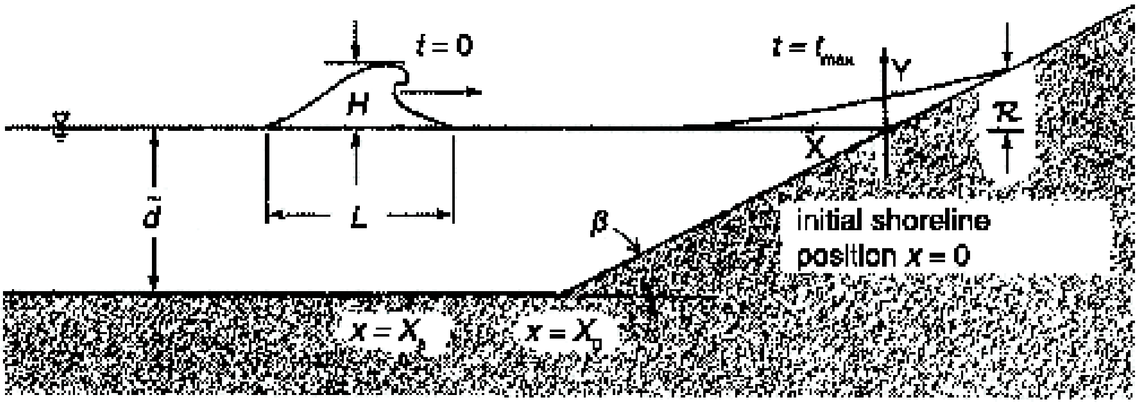

Figure 3.5 – Definition sketch for the canonical problem of a constant-depth region adjoining a sloping beach. Taken from Synolakis *et al.* (2007).

The test case was performed for two different waves with relative amplitudes of 0.0185 and 0.3. The wave with relative amplitude of 0.0185 is a non-breaking wave and the one a relative amplitude of 0.3 is a breaking wave.

Since the available laboratory data was presented scaled to match the target relative amplitudes rather than the measured results (i.e. initial wave height for both tests was 0.0185 m and 0.3 m respectively in the available laboratory data), the simulations on the numerical model were ran on an equivalent bathymetry with an 1 m deep tank, for A/h=0.0185, and a 10 m deep tank for A/h=0.3.

The results obtained from the numerical model and comparison with the laboratory data are presented from Figure 3.6 to Figure 3.10, for A/h=0.0185, and from Figure 3.11 to Figure 3.14, for A/h=0.3. These results correspond to snapshots of the wave profile for certain non-dimensional instants (i.e. simulation instants or simulation frames).

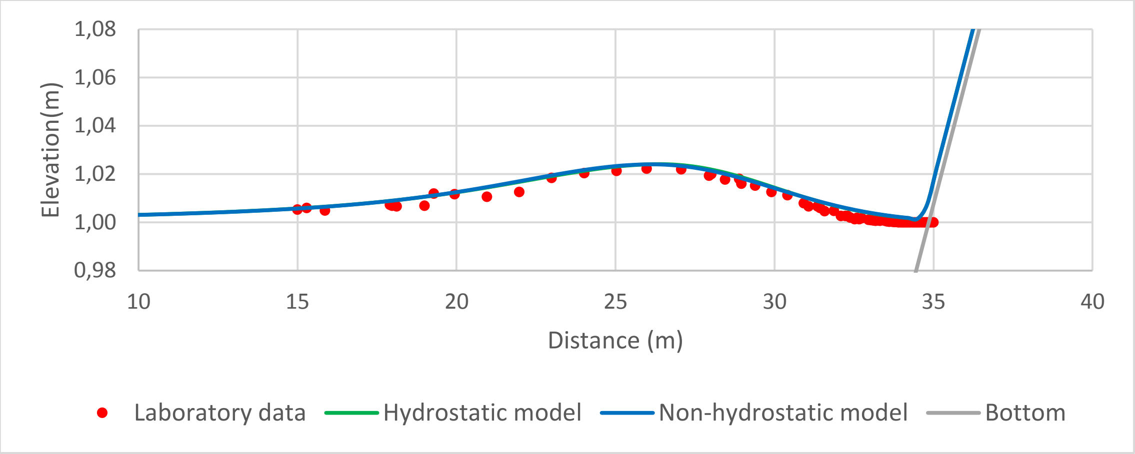

Figure 3.6 - Time evolution of a non-breaking wave with A/h = 0.0185, for T=30. Spatial step=0.3 m. Time step=0.05 s.

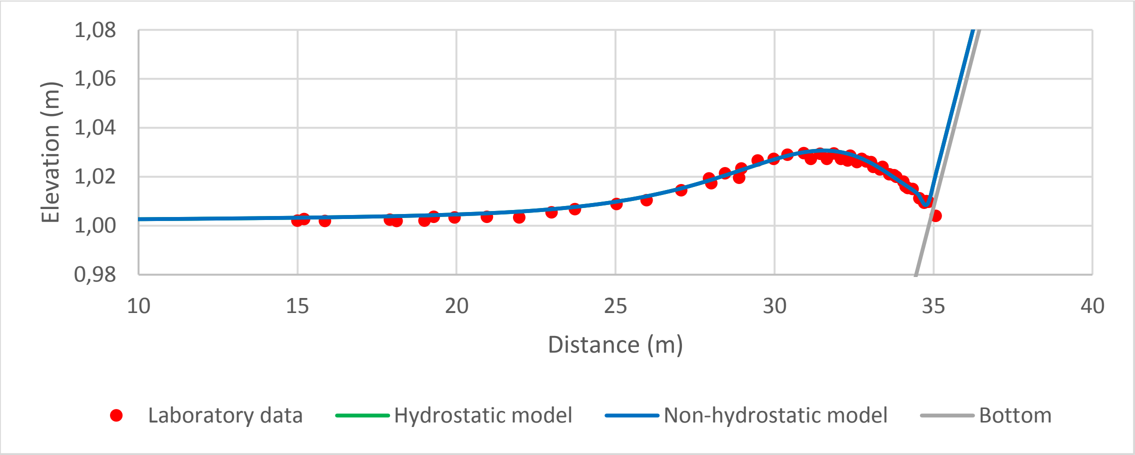

Figure 3.7 - Time evolution of a non-breaking wave with A/h = 0.0185, for T=40. Spatial step=0.3 m. Time step=0.05 s.

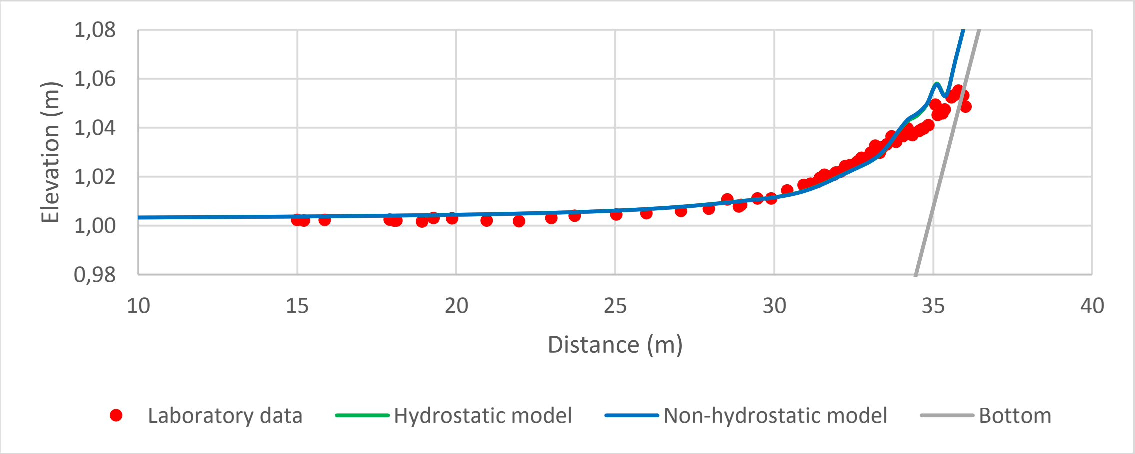

Figure 3.8 - Time evolution of a non-breaking wave with A/h = 0.0185, for T=50. Spatial step=0.3 m. Time step=0.05 s.

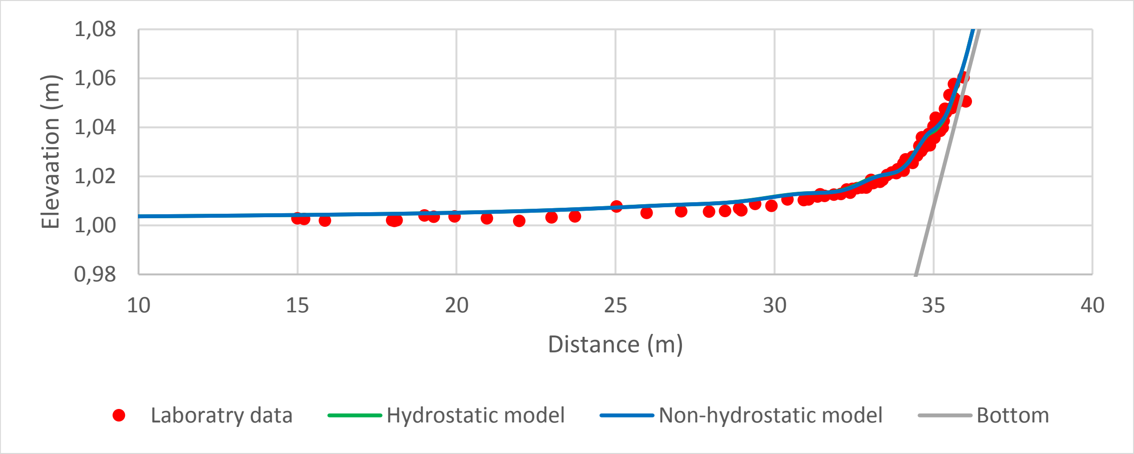

Figure 3.9 - Time evolution of a non-breaking wave with A/h = 0.0185, for T=60. Spatial step=0.3 m. Time step=0.05 s.

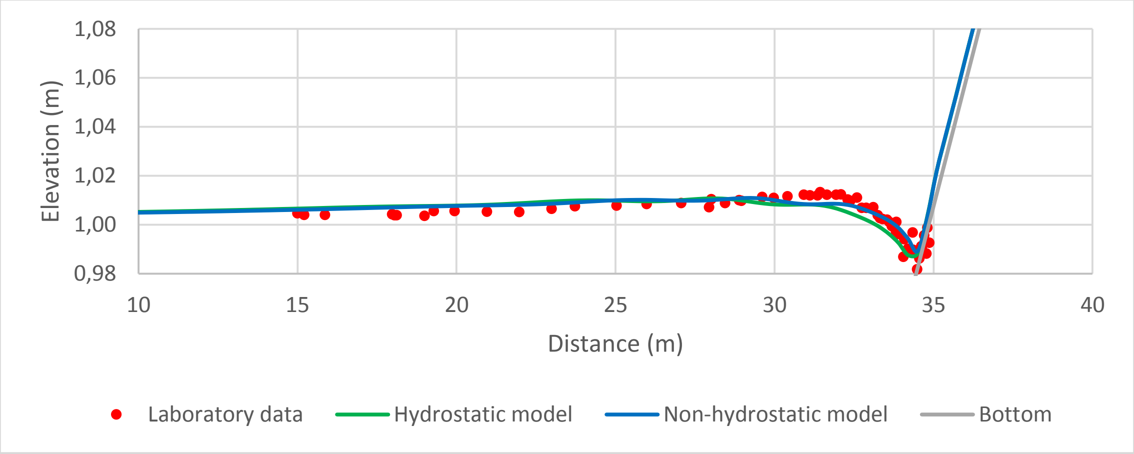

Figure 3.10 - Time evolution of a non-breaking wave with A/h = 0.0185, for T=70. Spatial step=0.3 m. Time step=0.05 s.

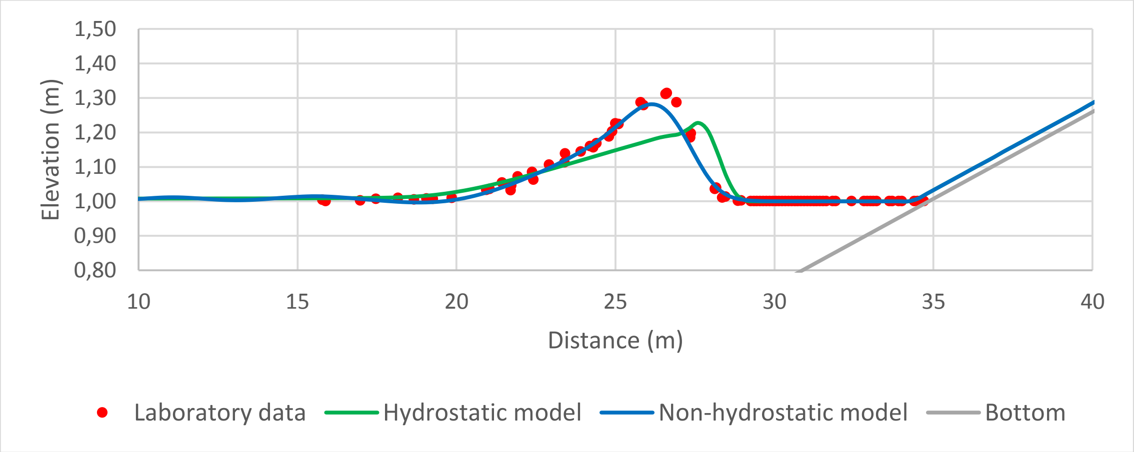

Figure 3.11 - Time evolution of a breaking wave with A/h = 0.3, for T=15. Spatial step=3 m. Time step=0.01 s.

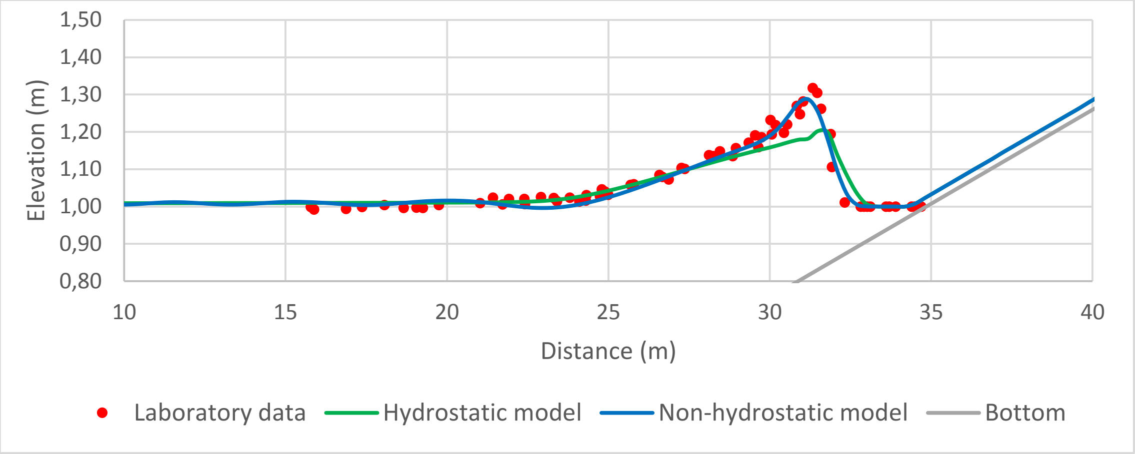

Figure 3.12 - Time evolution of a breaking a wave with A/h = 0.3, for T=20. Spatial step=3 m. Time step=0.01 s.

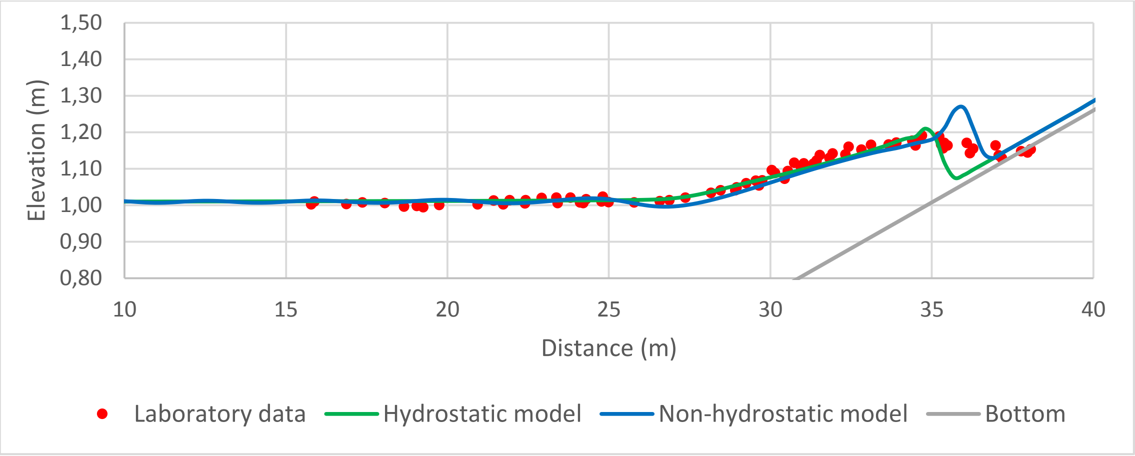

Figure 3.13 - Time evolution of a breaking a wave with A/h = 0.3, for T=25. Spatial step=3 m. Time step=0.01 s.

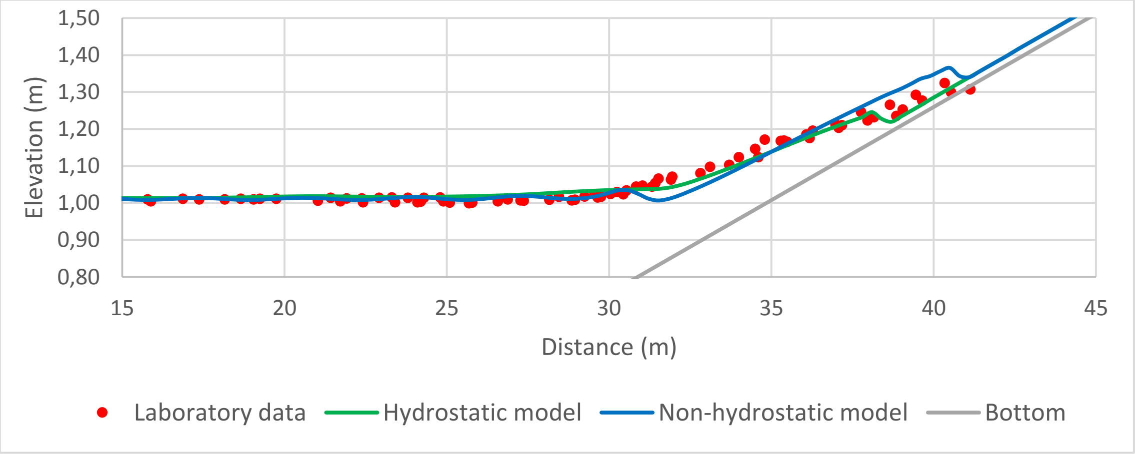

Figure 3.14 - Time evolution of a breaking a wave with A/h = 0.3, for T=30. Spatial step=3 m. Time step=0.01 s.

From the results, we can conclude that for the case of the non-breaking wave (A/h=0.0185) both models are equally accurate at simulating the wave propagation and run-up.

As for the case of the breaking wave (A/h=0.3), the hydrostatic model struggles to reproduce the wave profile obtained from the laboratory results and underestimates the maximum run-up. On the other hand, the non-hydrostatic model satisfactorily reproduces the maximum run-up and wave profile evolution for all cases except the instant shown in Figure 3.13. This suggests that the wave breaking module still needs further development.

3.2.2. SOLITARY WAVE ON A COMPOSITE BEACH

The objective of this test is to reproduce the laboratory results obtained for the propagation of solitary waves in a wave tank modelled after Revere Beach (Boston, Massachusetts).

The test was performed for 3 solitary waves with relative amplitudes of 0.039, 0.264 and 0.696 with a water depth of 21.8 cm at the flat bottom portion of the channel.

The physical model consists of a 23.2 m-long by 45 cm-wide glass-walled flume. The bathymetry was composed by a flat bottom section followed by three linear slopes of 1:53, 1:150 and 1:13 from seaward to shoreward with a vertical wall at the shoreline. A schematic of the physical model is presented in Figure 3.15.

Wave gauges placed along the flume (numbered from 1 to 10 in Figure 3.15) measured surface wave elevations for each trial and the gathered data was compared to the results produced by the numerical model. More details can be found in Appendix A of Synolakis *et al.* (2007) and US Army Corps of Engineers (2016).

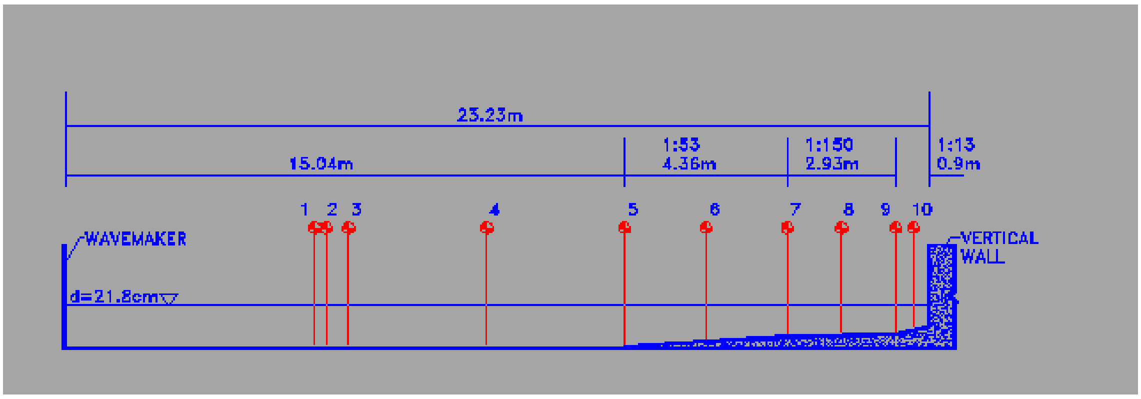

Figure 3.15 – Schematic of flume and gauge layout for the physical model of Revere Beach. Taken from US Army Corps of Engineers (2016).

The results obtained in the numerical simulations and respective comparison with the laboratory data are presented below, from Figure 3.16 to Figure 3.22 for A/h=0.039, from Figure 3.23 to Figure 3.29 for A/h=0.264, and from Figure 3.30 to Figure 3.36 for A/h=0.696.

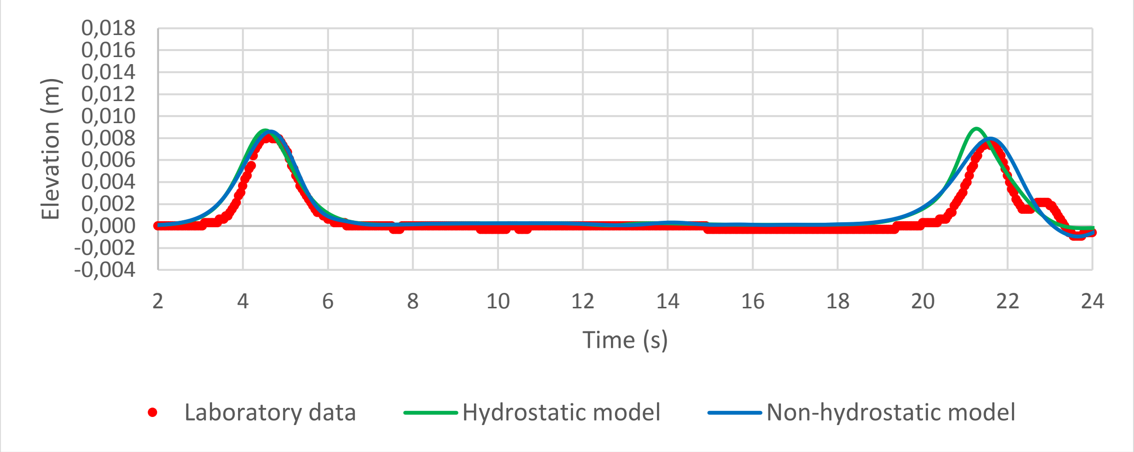

Figure 3.16 - Time evolution of a non-breaking wave, with initial A/h=0.039, on a composite beach. Gauge 4. Spatial step=0.12 m. Time step=0.02 s.

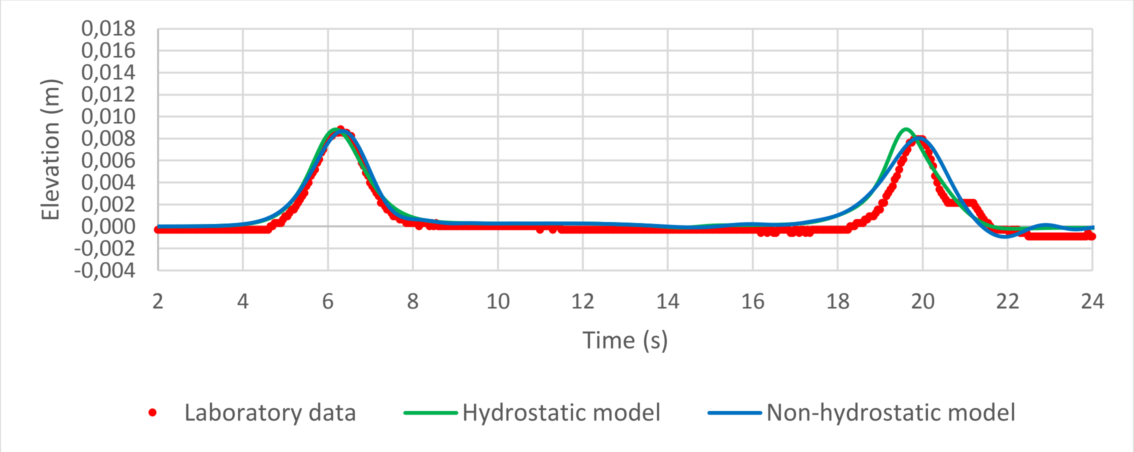

Figure 3.17 - Time evolution of a non-breaking wave, with initial A/h=0.039, on a composite beach. Gauge 5. Spatial step=0.12 m. Time step=0.02 s.

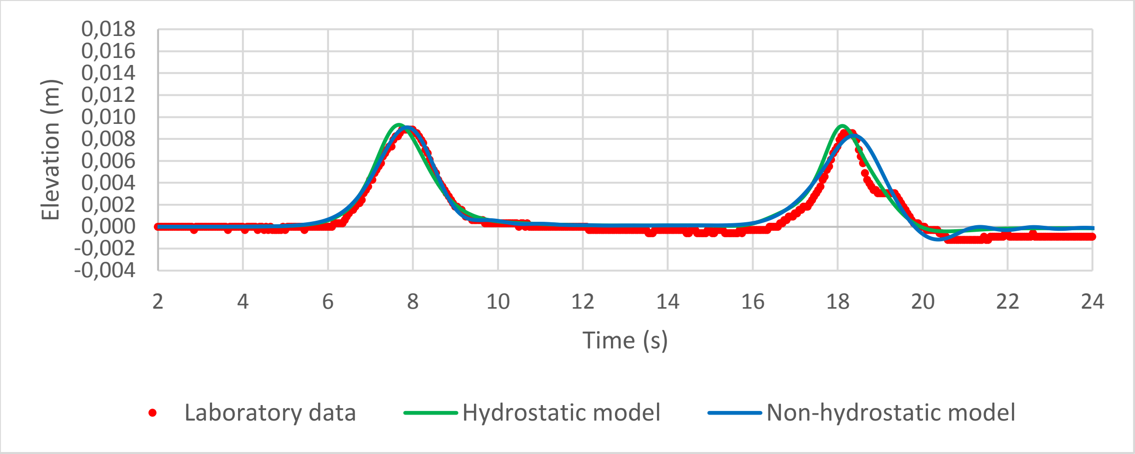

Figure 3.18 - Time evolution of a non-breaking wave, with initial A/h=0.039, on a composite beach. Gauge 6. Spatial step=0.12 m. Time step=0.02 s.

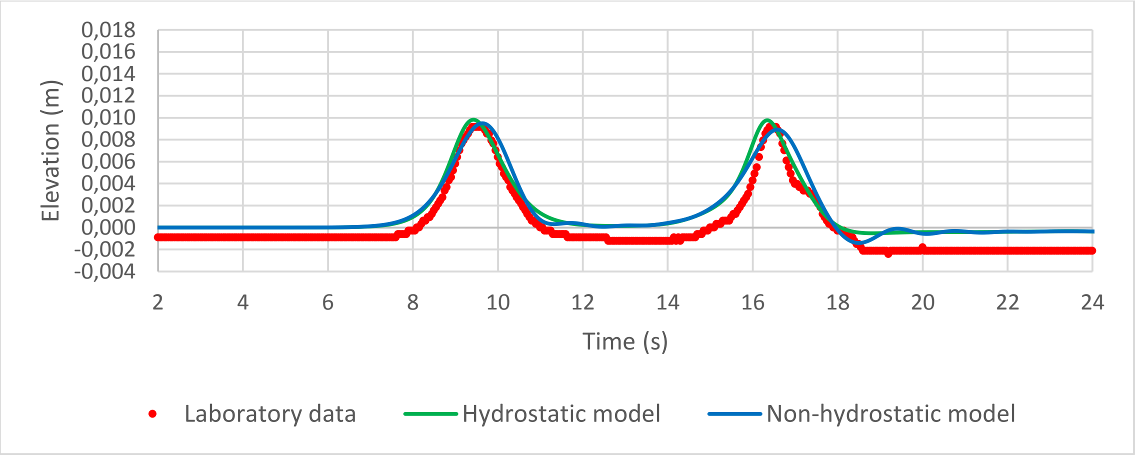

Figure 3.19 - Time evolution of a non-breaking wave, with initial A/h=0.039, on a composite beach. Gauge 7. Spatial step=0.12 m. Time step=0.02 s.

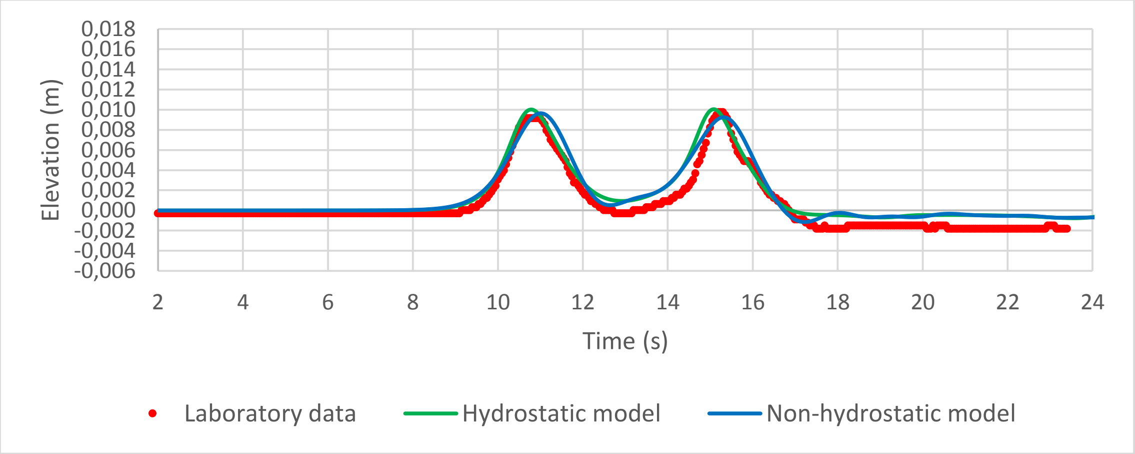

Figure 3.20 - Time evolution of a non-breaking wave, with initial A/h=0.039, on a composite beach. Gauge 8. Spatial step=0.12 m. Time step=0.02 s.

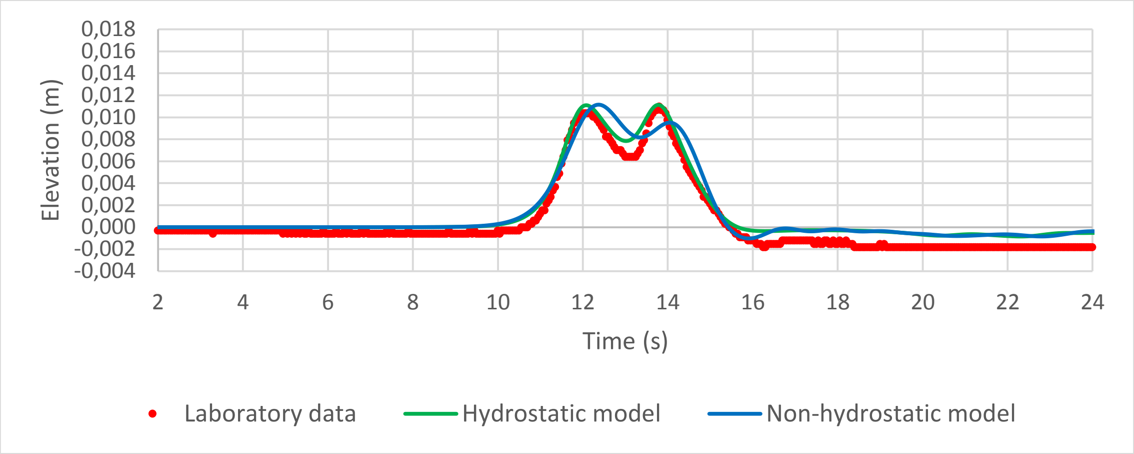

Figure 3.21 - Time evolution of a non-breaking wave, with initial A/h=0.039, on a composite beach. Gauge 9. Spatial step=0.12 m. Time step=0.02 s.

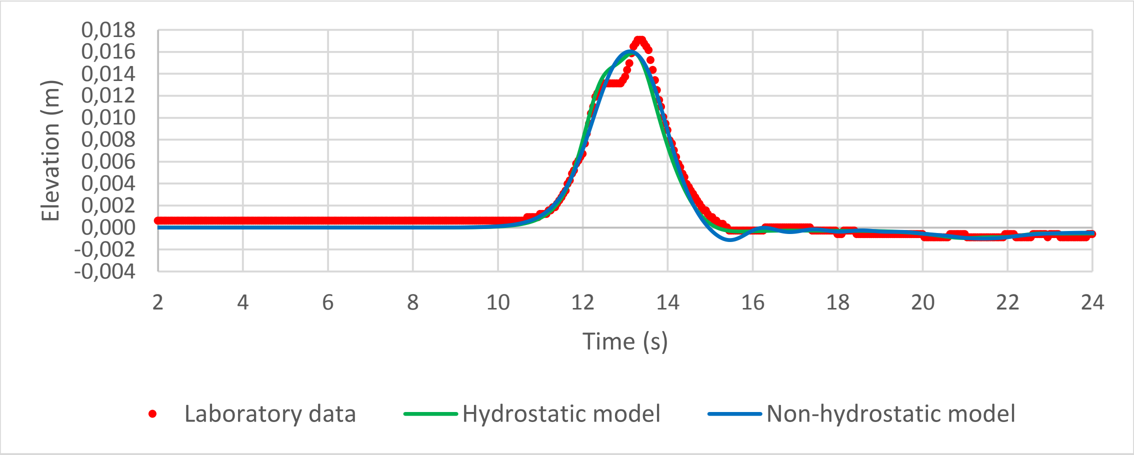

Figure 3.22 - Time evolution of a non-breaking wave, with initial A/h=0.039, on a composite beach. Gauge 10. Spatial step=0.12 m. Time step=0.02 s.

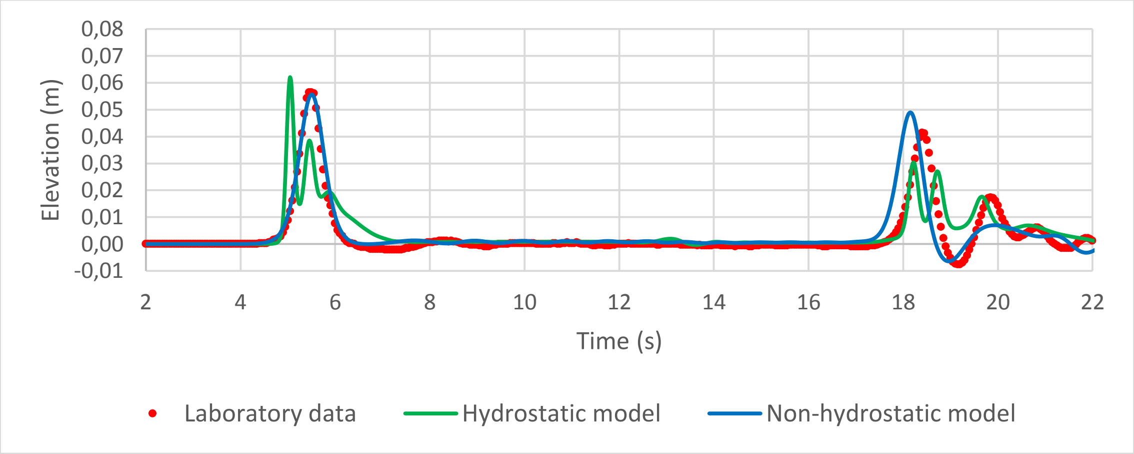

Figure 3.23 - Time evolution of a breaking wave, with initial A/h=0.264, on a composite beach. Gauge 4. Spatial step=1.2 m. Time step=0.02 s.

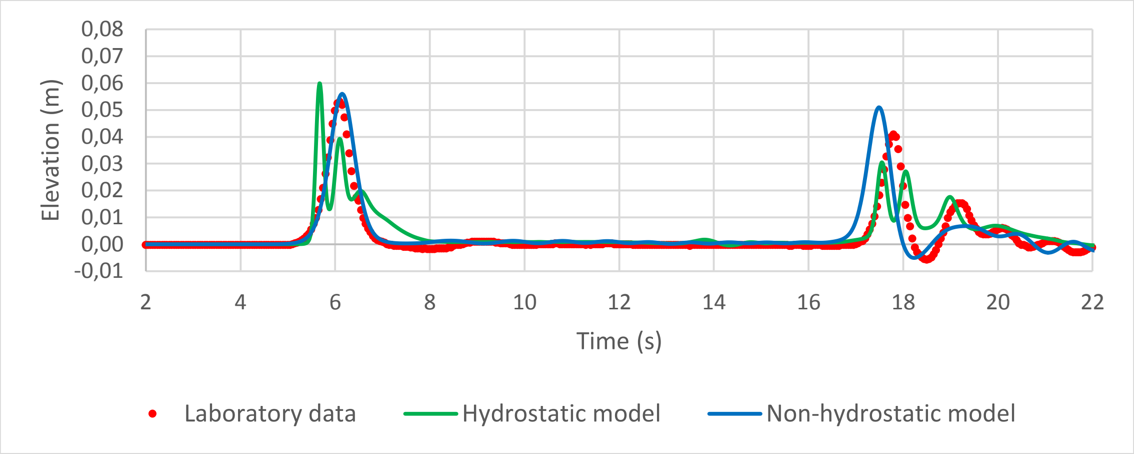

Figure 3.24 - Time evolution of a breaking wave, with initial A/h=0.264, on a composite beach. Gauge 5. Spatial step=1.2 m. Time step=0.02 s.

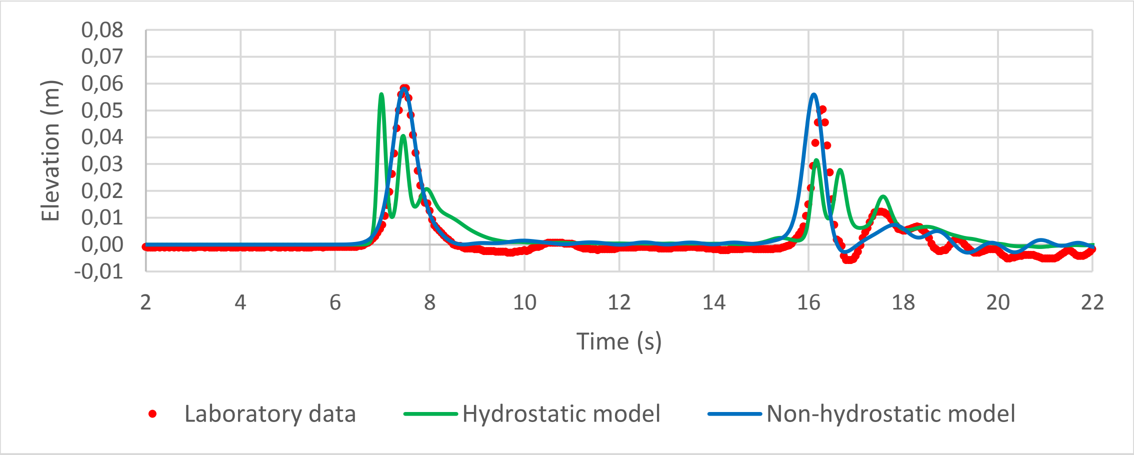

Figure 3.25 - Time evolution of a breaking wave, with initial A/h=0.264, on a composite beach. Gauge 6. Spatial step=1.2 m. Time step=0.02 s.

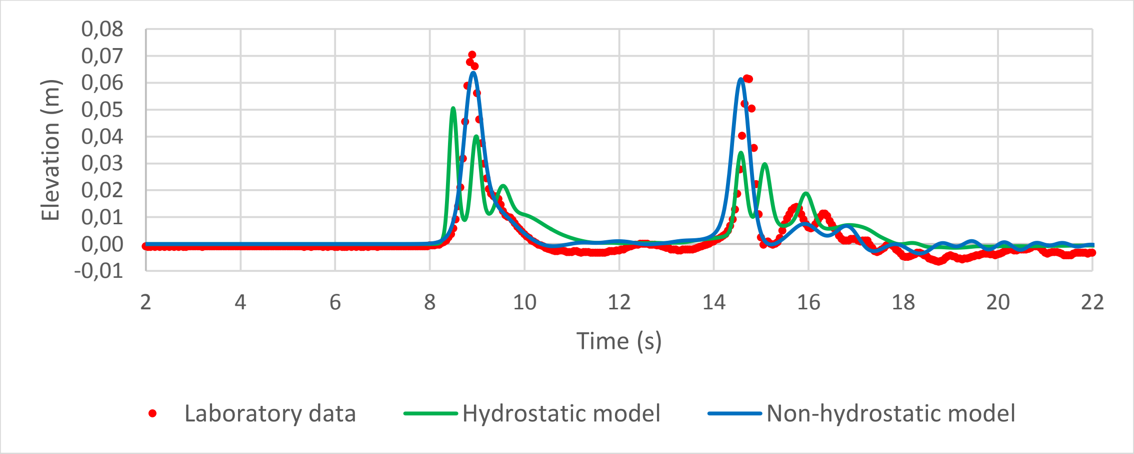

Figure 3.26 - Time evolution of a breaking wave, with initial A/h=0.264, on a composite beach. Gauge 7. Spatial step=1.2 m. Time step=0.02 s.

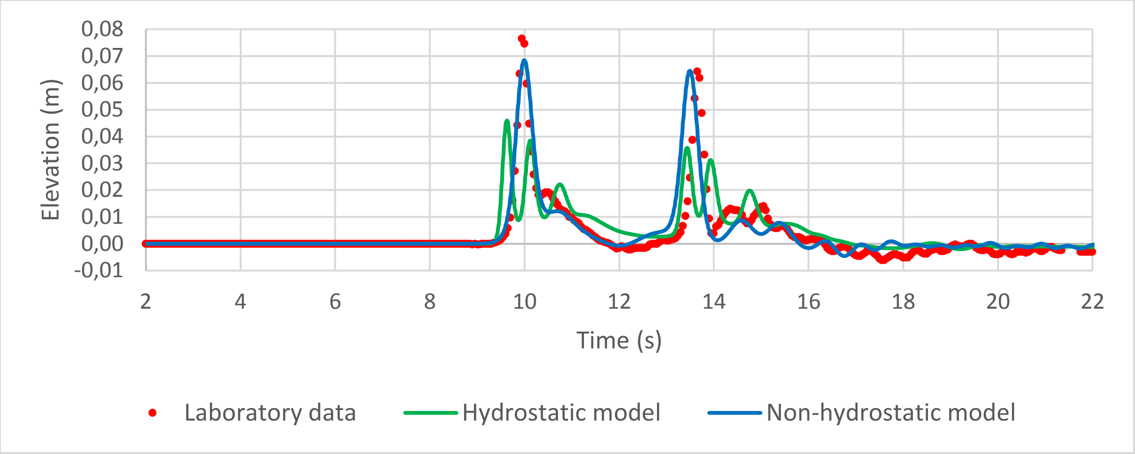

Figure 3.27 - Time evolution of a breaking wave, with initial A/h=0.264, on a composite beach. Gauge 8. Spatial step=1.2 m. Time step=0.02 s.

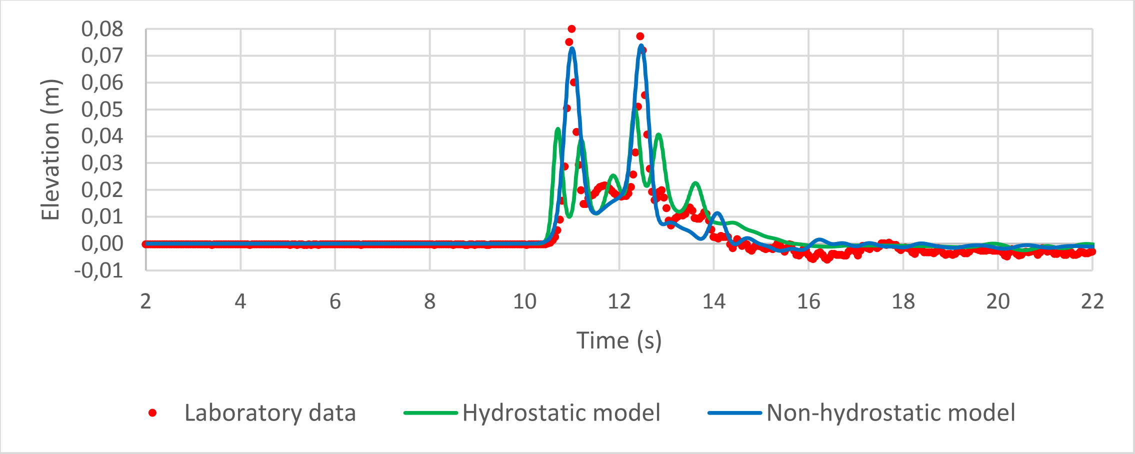

Figure 3.28 - Time evolution of a breaking wave, with initial A/h=0.264, on a composite beach. Gauge 9. Spatial step=1.2 m. Time step=0.02 s.

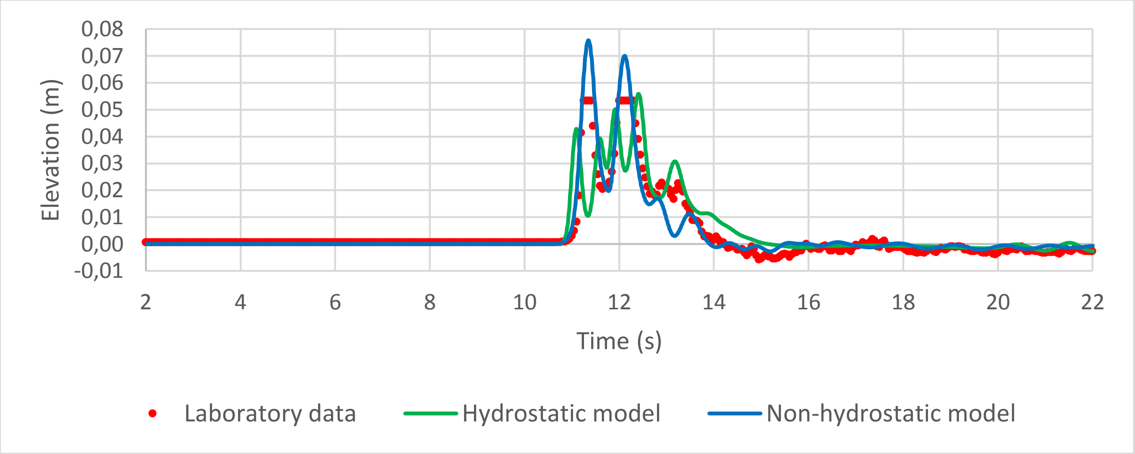

Figure 3.29 - Time evolution of a breaking wave, with initial A/h=0.264, on a composite beach. Gauge 10. Spatial step=1.2 m. Time step=0.02 s.

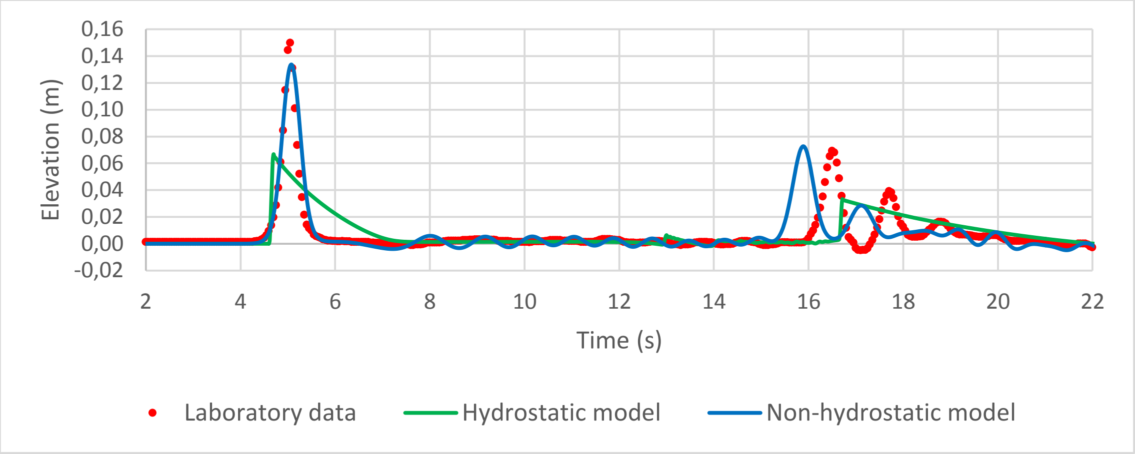

Figure 3.30 - Time evolution of a breaking wave, with initial A/h=0.696, on a composite beach. Gauge 4. Spatial step=0.12 m. Time step=0.0001 s.

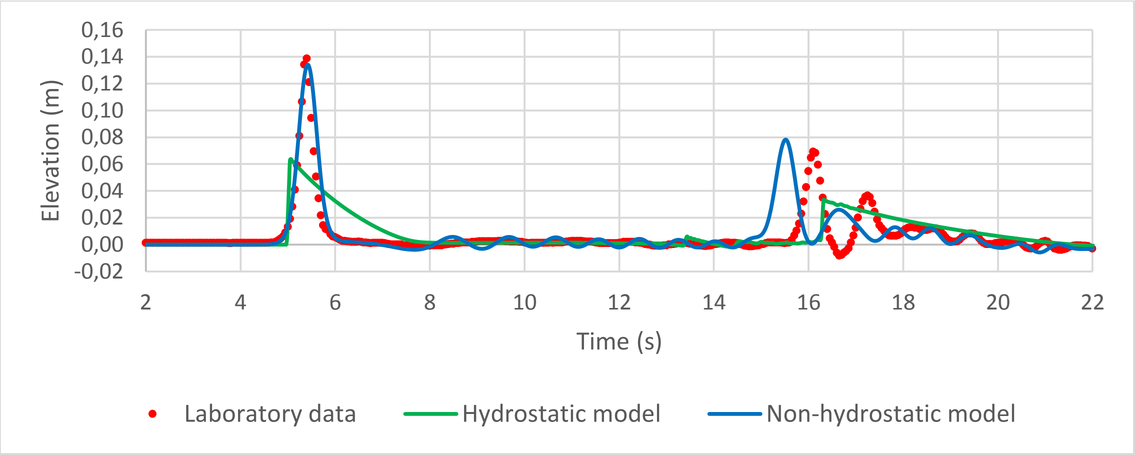

Figure 3.31 - Time evolution of a breaking wave, with initial A/h=0.696, on a composite beach. Gauge 5. Spatial step=0.12 m. Time step=0.0001 s.

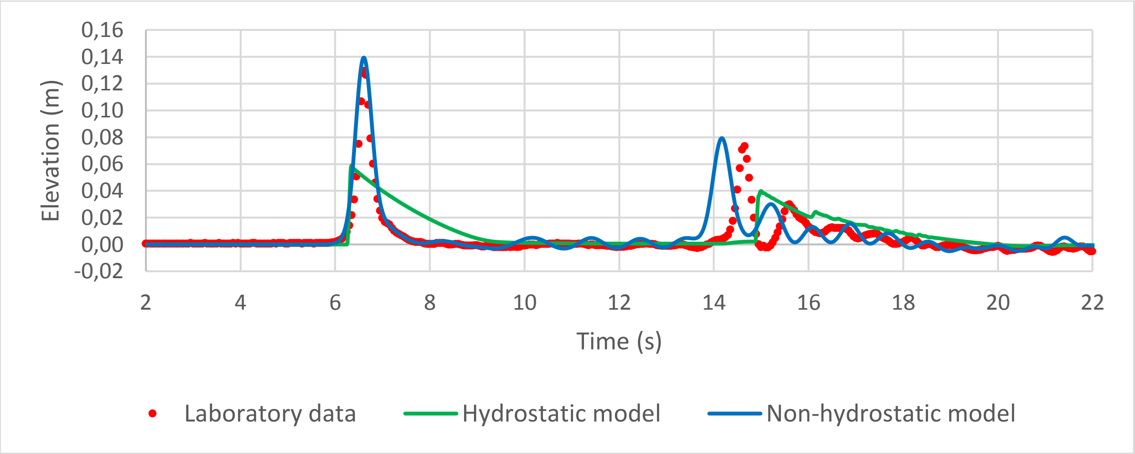

Figure 3.32 - Time evolution of a breaking wave, with initial A/h=0.696, on a composite beach. Gauge 6. Spatial step=0.12 m. Time step=0.0001 s.

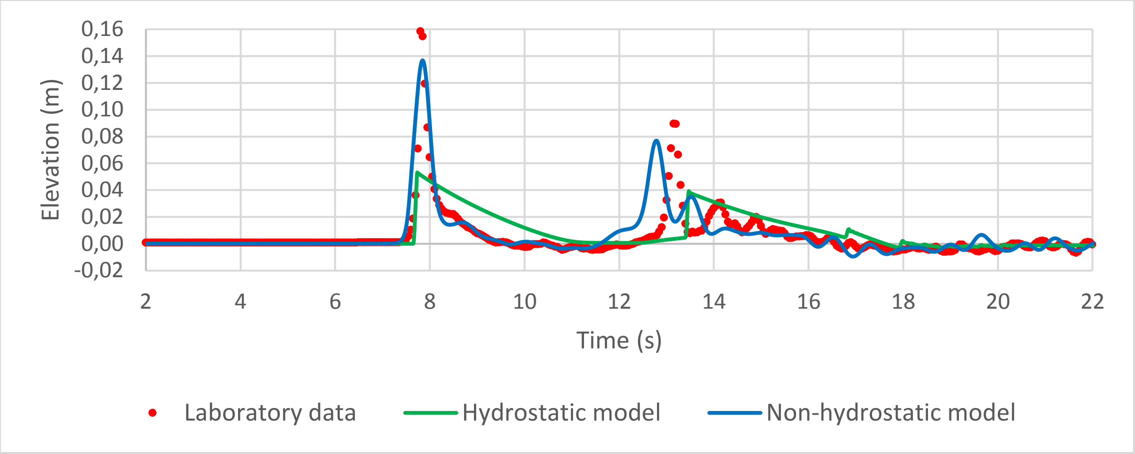

Figure 3.33 - Time evolution of a breaking wave, with initial A/h=0.696, on a composite beach. Gauge 7. Spatial step=0.12 m. Time step=0.0001 s.

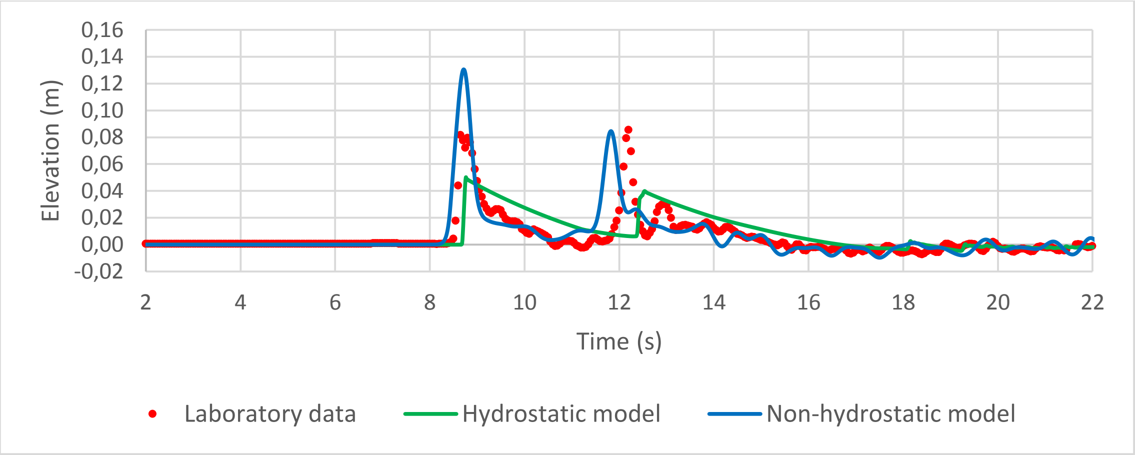

Figure 3.34 - Time evolution of a breaking wave, with initial A/h=0.696, on a composite beach. Gauge 8. Spatial step=0.12 m. Time step=0.0001 s.

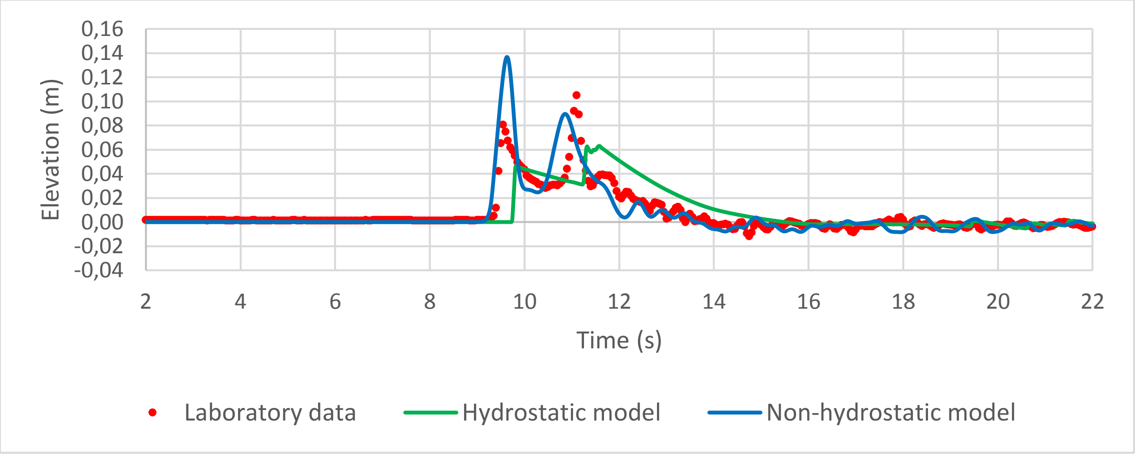

Figure 3.35 - Time evolution of a breaking wave, with initial A/h=0.696, on a composite beach. Gauge 9. Spatial step=0.12 m. Time step=0.0001 s.

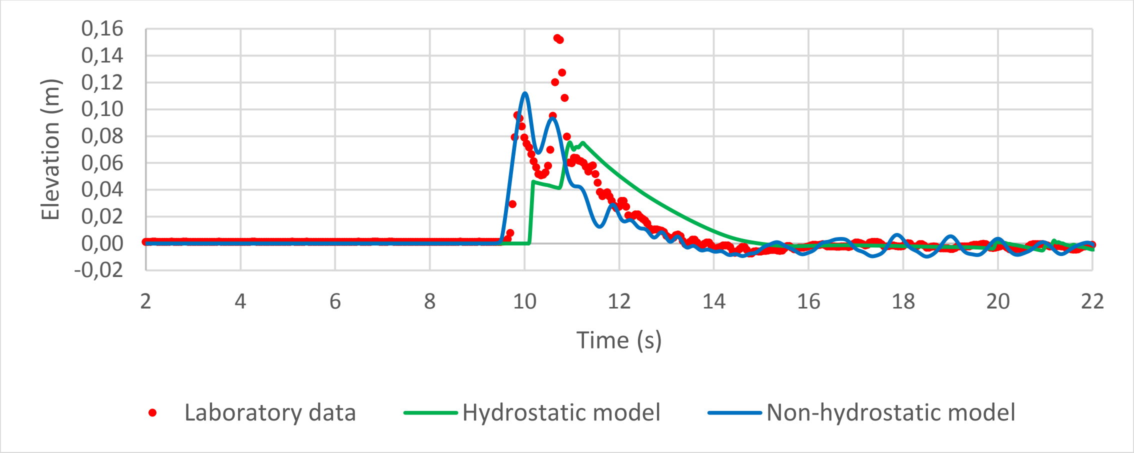

Figure 3.36 - Time evolution of a breaking wave, with initial A/h=0.696, on a composite beach. Gauge 10. Spatial step=0.12 m. Time step=0.0001 s.

Looking at the results for the composite beach test cases, it should be noted that for A/h=0.039 the exact initial wave profile was not possible to replicate. Nevertheless, for this case both models display competent results in their simulations, with the hydrostatic model actually being more accurate than the non-hydrostatic model up to the 18 sec mark, when the wave profile starts getting distorted and phase mismatch becomes noticeable.

For the cases of A/h=0.264 and A/h=0.696, the hydrostatic model fails to reproduce the correct wave profile with the wave breaking up and assuming several peaks in the first case, and in the second case assuming a very defined triangular shape. This difference may be attributed to the difference in time steps for both runs, since for the case of A/H=0.696 a very small time step was required to achieve model stability.

Looking at the non-hydrostatic model, the correct wave profile is reproduced much more accurately. Nevertheless, wave amplitude is overestimated or underestimated at certain points within a range of approximately +-10% of the measured wave profile, for most cases. The wave's propagation, in terms of phase, is well simulated up until reflecting against the vertical wall. From there, the simulated wave travels ahead of the measured data, with this result being more noticeable for the higher values of relative amplitude.

3.2.3. SOLITARY WAVE ON A CONICAL ISLAND

Motivated by the catastrophe in Babi Island, Indonesia during the 1992 Flores Island tsunami, large scale laboratory experiments were performed at the Coastal Engineering Research Center in Vicksburg, Mississippi, in a 30 m-wide, 25 m-long, and 60 cm-deep wave basin (Briggs *et al.* 1995) (Synolakis *et al.* 2007). At the centre of the basin was an island with the shape of a truncated, right circular cone with diameters of 7.2 m at the toe and 2.2 m at the crest. The vertical height of the island was approximately 62.5 cm with a slope of 1:4 on its beach face. The objective of the experiments was to study the run-up process of a tsunami on a circular island.

A definition sketch for the profile of the conical island is presented in Figure 3.37 and more details on the physical model and experiments can be found in Appendix A of Synolakis *et al.* (2007) and US Army Corps of Engineers (2016).

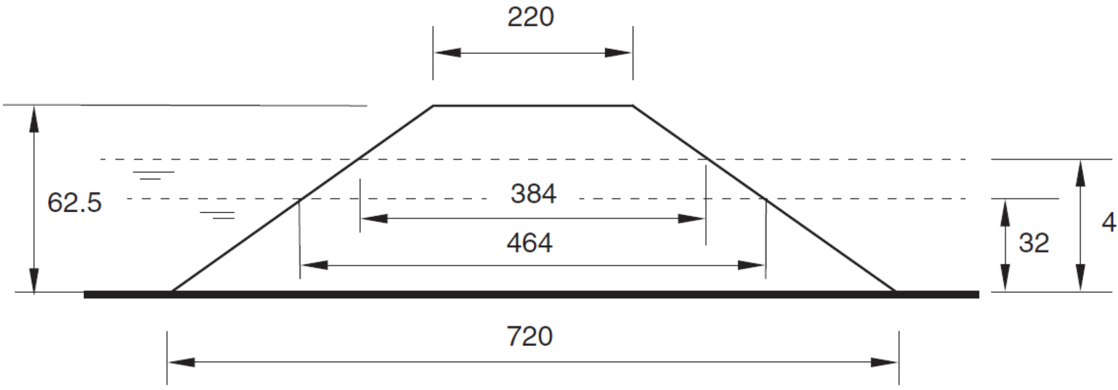

Figure 3.37 – Definition sketch of the conical island. Dimensions in centimetres. Not to scale. Taken from Synolakis *et al.* (2007)

This set of experiments has been used in several validation studies for a variety of models, such as non-linear shallow water equations (Liu *et al.* 1995) and Boussinesq equations (Chen *et al.* 2000).

Using a 100:1 bathymetry based on the physical model, several simulation trials were ran for solitary waves with relative amplitudes of 0.045, 0.096 and 0.181. The results generated by the numerical models were then compared with the time series generated by several wave gauges placed around the beach face of the conical island. The disposition of the wave gauges can be seen in Figure 3.38. The comparative analysis was done for the data recorded by gauges 6, 9, 16 and 22 and is presented from Figure 3.39 to Figure 3.42 for A/h=0.045, from Figure 3.43 to Figure 3.46 for A/h=0.096 and from Figure 3.47 to Figure 3.50 for A/h=0.181.

The maximum run-up values around the island, computed by the numerical models, and respective comparison with the laboratory data are presented from Figure 3.51 to Figure 3.53.

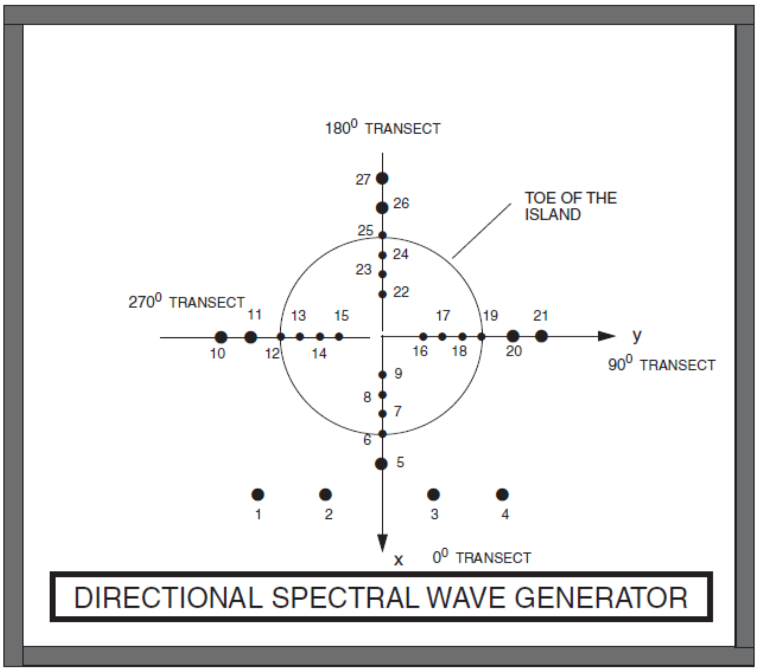

Figure 3.38 – Schematic of the placement of the wave gauges around the beach face of the conical island. Taken from Synolakis *et al.* (2007).

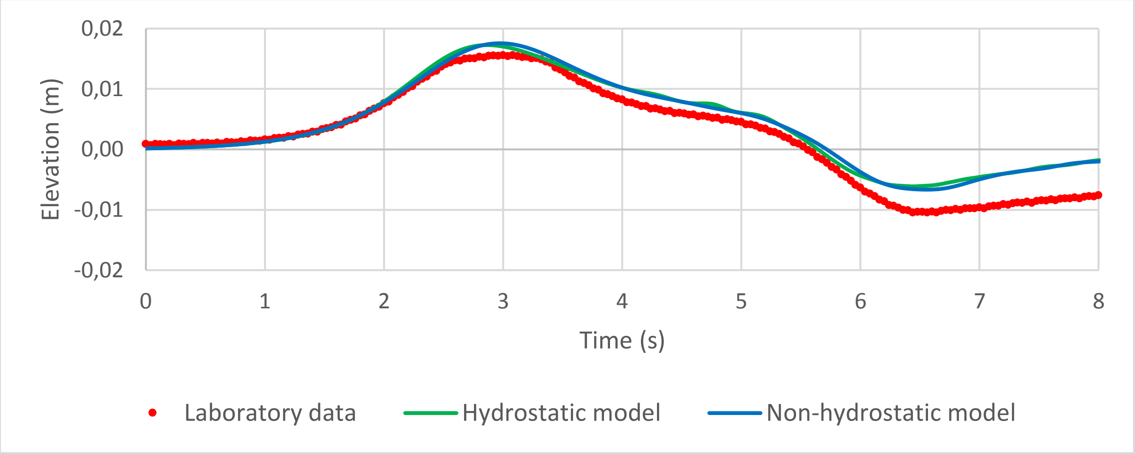

Figure 3.39 - Comparison between computed and measured time series, on the conical island wave tank, for A/h=0.045. Gauge 6. Spatial step=5 m. Time step=0.01 s.

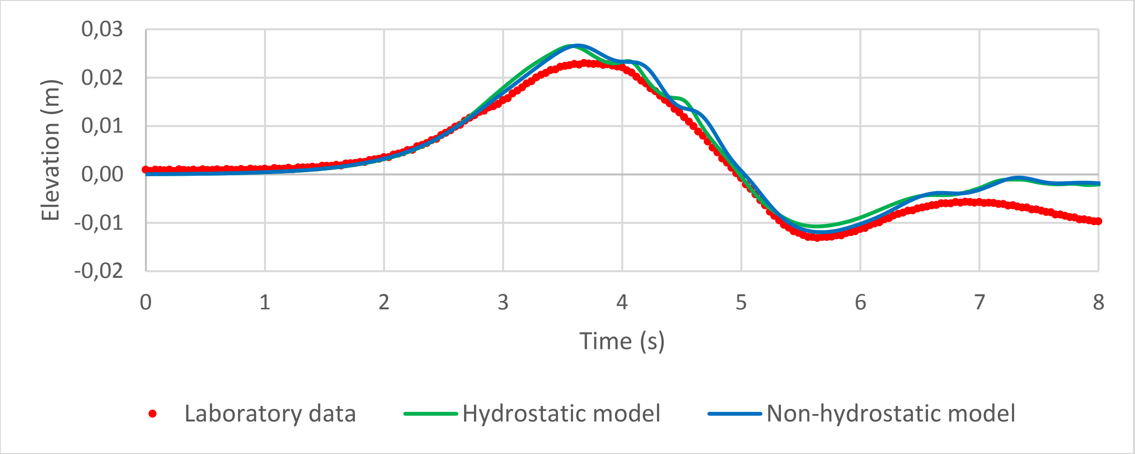

Figure 3.40 - Comparison between computed and measured time series, on the conical island wave tank, for A/h=0.045. Gauge 9. Spatial step=5 m. Time step=0.01 s.

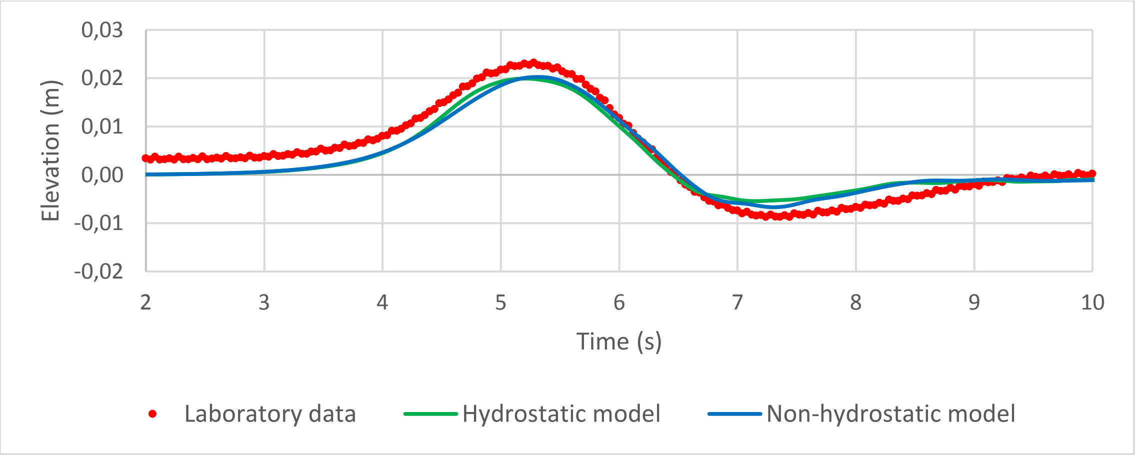

Figure 3.41 - Comparison between computed and measured time series, on the conical island wave tank, for A/h=0.045. Gauge 16. Spatial step=5 m. Time step=0.01 s.

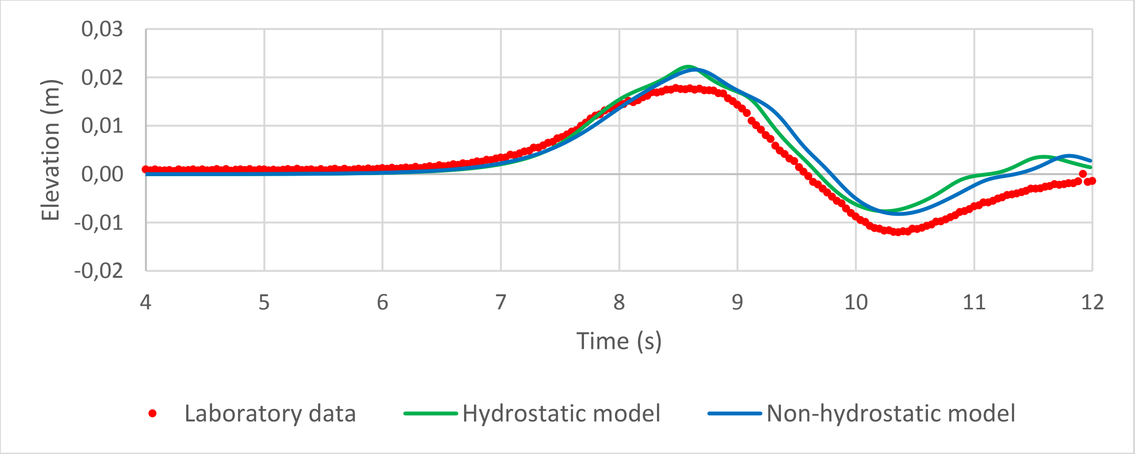

Figure 3.42 - Comparison between computed and measured time series, on the conical island wave tank, for A/h=0.045. Gauge 22. Spatial step=5 m. Time step=0.01 s.

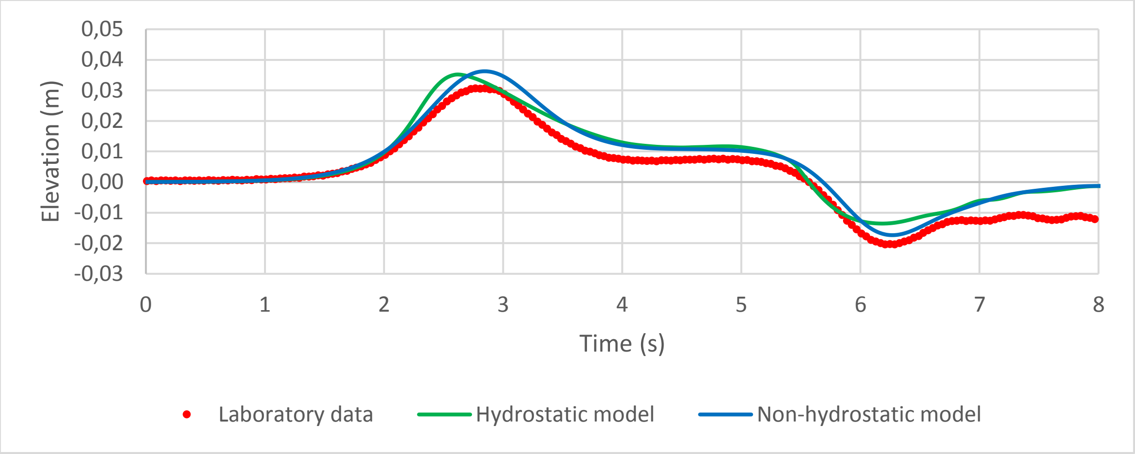

Figure 3.43 - Comparison between computed and measured time series, on the conical island wave tank, for A/h=0.096. Gauge 6. Spatial step=5 m. Time step=0.01 s.

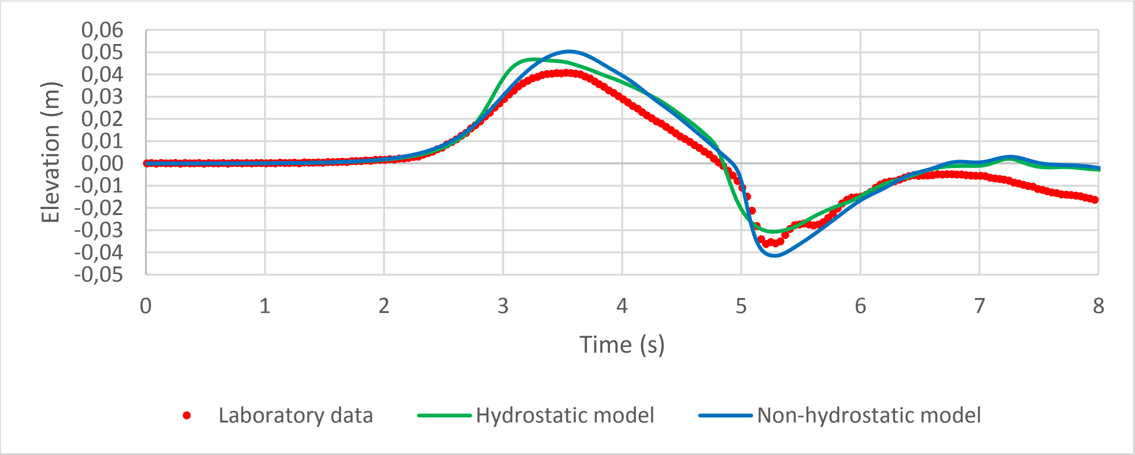

Figure 3.44 - Comparison between computed and measured time series, on the conical island wave tank, for A/h=0.096. Gauge 9. Spatial step=5 m. Time step=0.01 s.

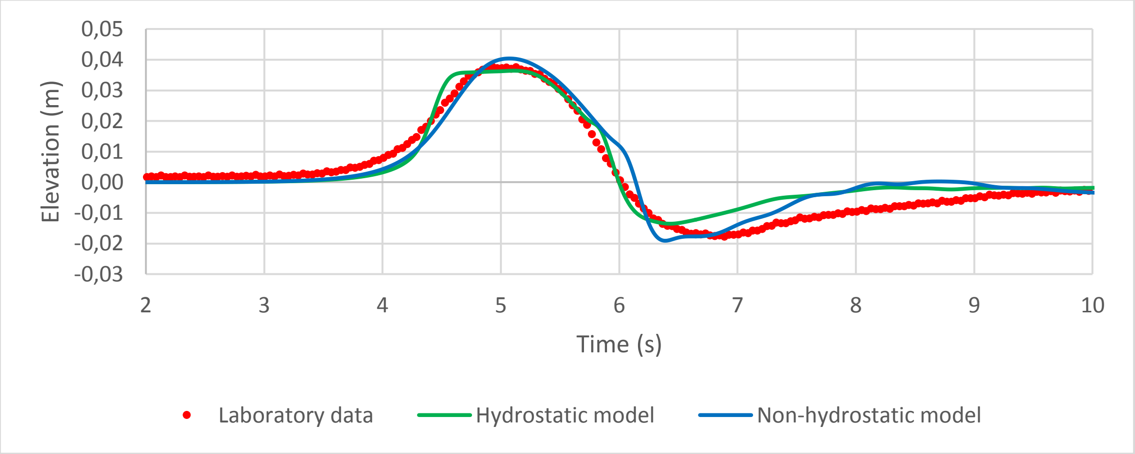

Figure 3.45 - Comparison between computed and measured time series, on the conical island wave tank, for A/h=0.096. Gauge 16. Spatial step=5 m. Time step=0.01 s.

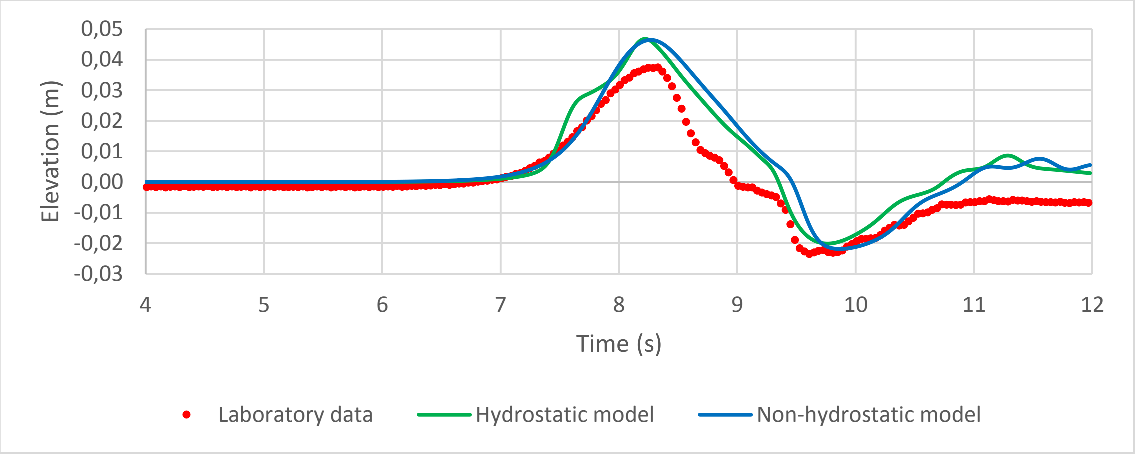

Figure 3.46 - Comparison between computed and measured time series, on the conical island wave tank, for A/h=0.096. Gauge 22. Spatial step=5 m. Time step=0.01 s.

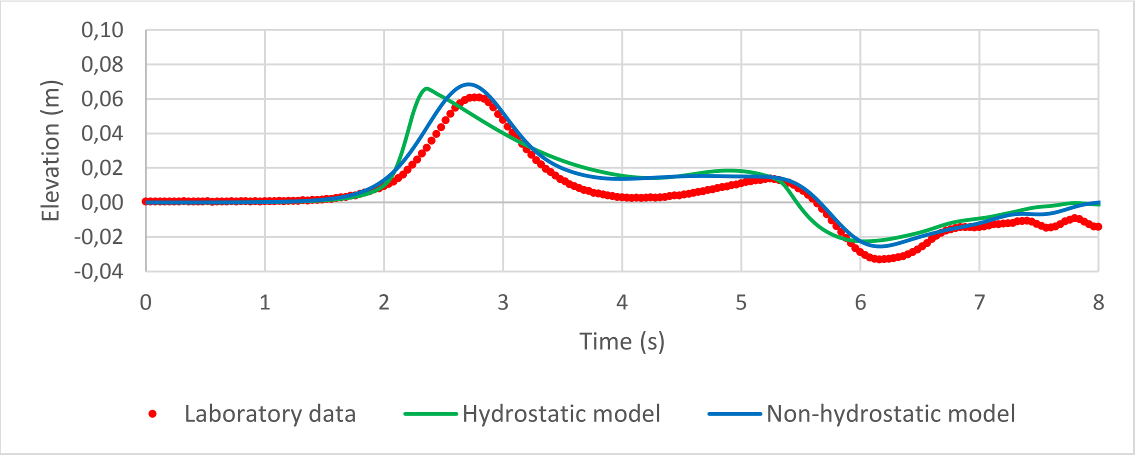

Figure 3.47 - Comparison between computed and measured time series, on the conical island wave tank, for A/h=0.181. Gauge 6. Spatial step=5 m. Time step=0.01 s.

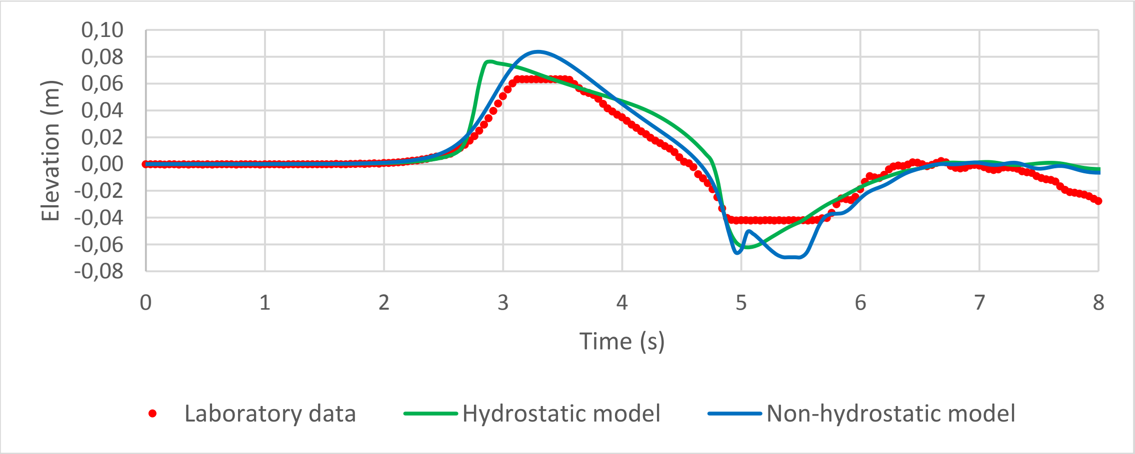

Figure 3.48 - Comparison between computed and measured time series, on the conical island wave tank, for A/h=0.181. Gauge 9. Spatial step=5 m. Time step=0.01 s.

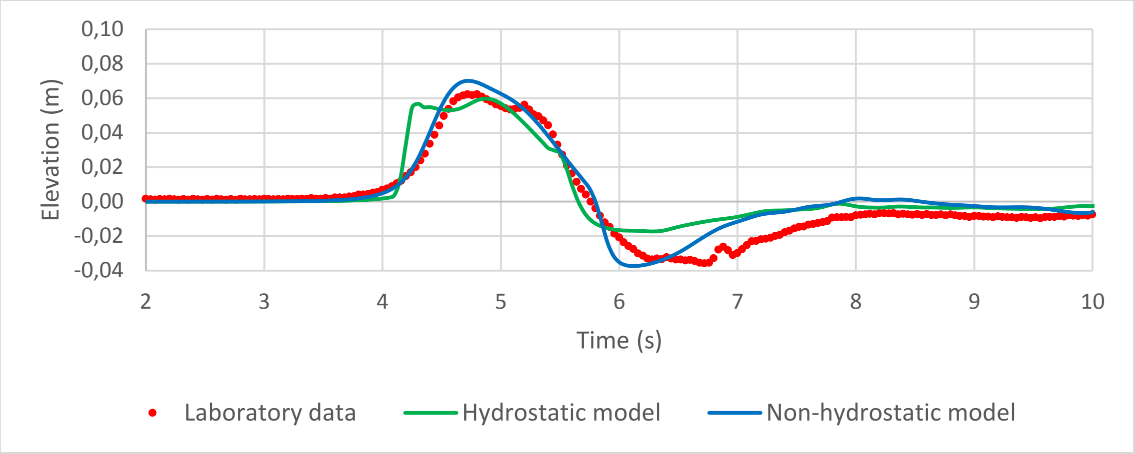

Figure 3.49 - Comparison between computed and measured time series, on the conical island wave tank, for A/h=0.181. Gauge 16. Spatial step=5 m. Time step=0.01 s.

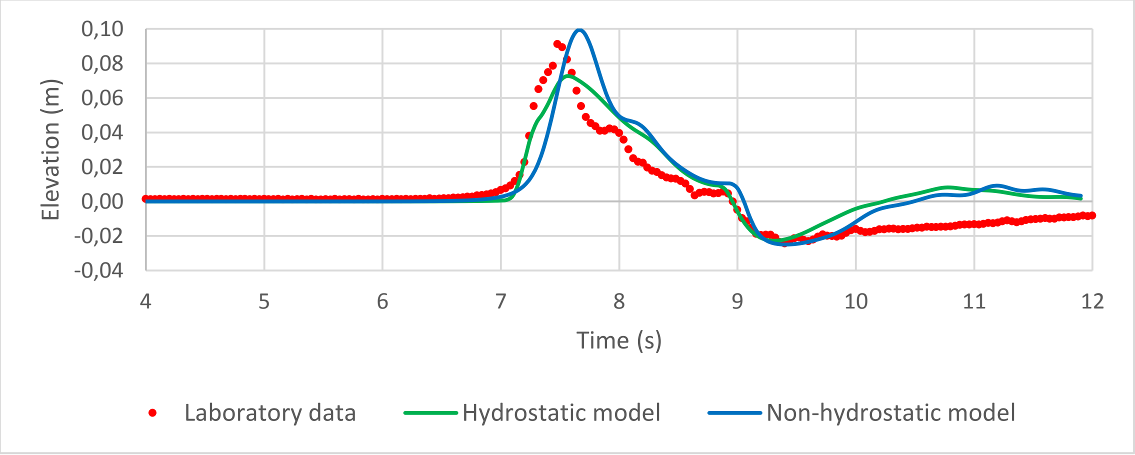

Figure 3.50 - Comparison between computed and measured time series, on the conical island wave tank, for A/h=0.181. Gauge 22. Spatial step=5 m. Time step=0.01 s.

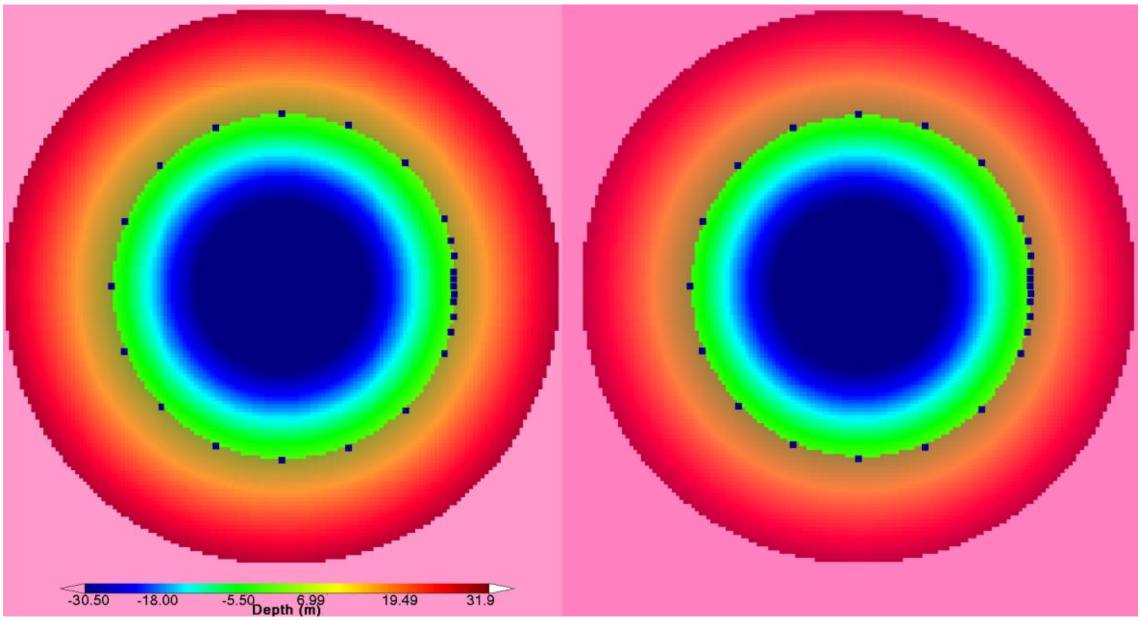

Figure 3.51 – Comparison of the maximum run-up around the conical island, for A/h=0.045, between the computed results for the non-hydrostatic (left) and hydrostatic (right) models and measured data (blue squares).

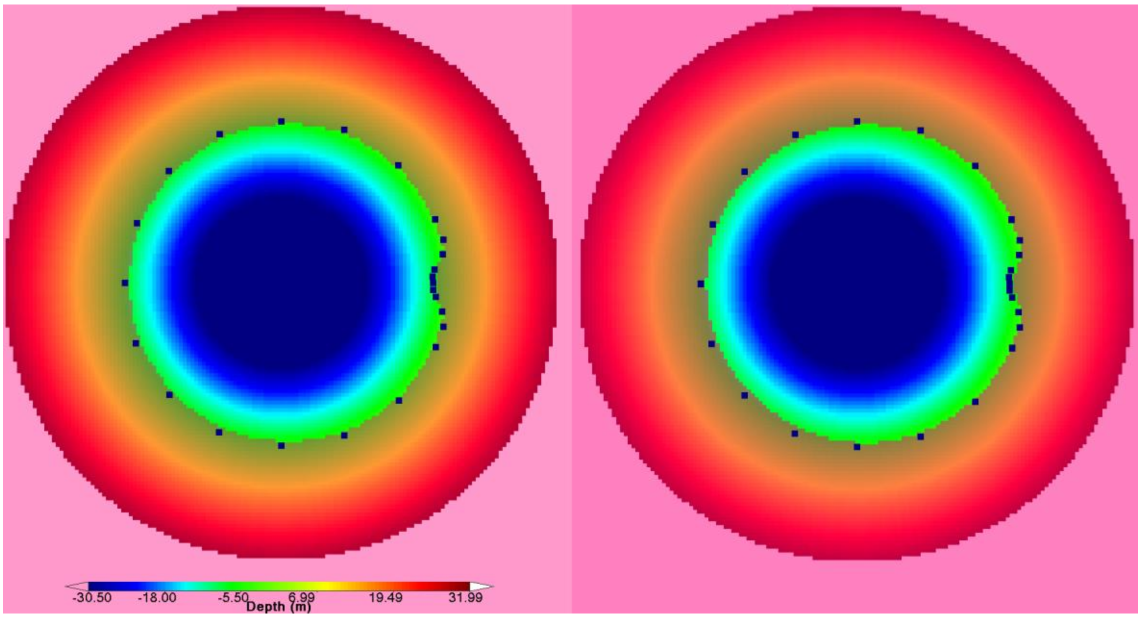

Figure 3.52 – Comparison of the maximum run-up around the conical island, for A/h=0.096, between the computed results for the non-hydrostatic (left) and hydrostatic (right) models and measured data (blue squares).

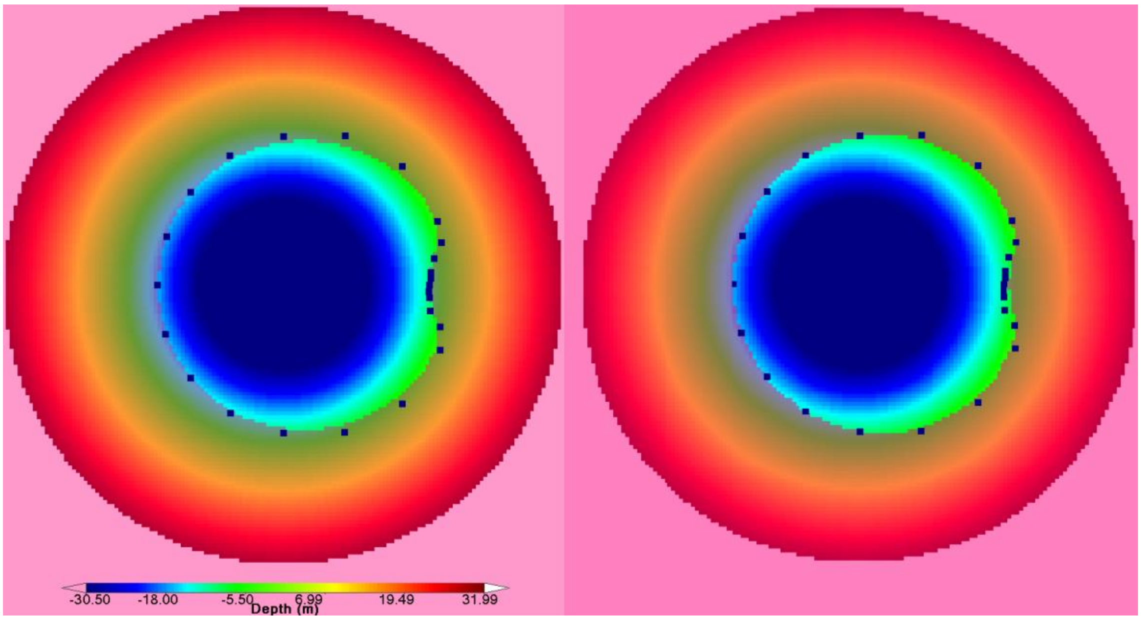

Figure 3.53 – Comparison of the maximum run-up around the conical island, for A/h=0.181, between the computed results for the non-hydrostatic (left) and hydrostatic (right) models and measured data (blue squares).

For the conical island test case, both models produce competent results. When it comes to the wave evolution, the non-hydrostatic model is more accurate at calculating the correct wave profile, especially at the back of the island (relative to wave direction). The phase evolution is well simulated in both models.

Looking at the maximum run-up, at the front of the island the simulated results are well adjusted with the recorded data for both models. At the back side of the island, for A/h=0.181 and, to less degree, for A/h=0.096, the hydrostatic model underestimates the maximum run-up while the non-hydrostatic model has a good adjustment.

3.2.4. TSUNAMI RUN-UP ONTO A COMPLEX THREE-DIMENSIONAL BEACH; MONAI VALLEY

Monai Valley is a region of Okushiri Island, Japan, hit by the Hokkaido-Nansei-Oki tsunami of 1993. Associated with this event, currents of the order of 10-18 m/s were recorded as well as an extreme run-up height of 30 m at the tip of a very narrow gulley within a small cove (Synolakis *et al.* 2007).

From a scientific point of view this tsunami was particularly interesting for the high-quality data it provided. Due to the existence of high resolution bathymetry before the event, it was possible to meaningfully identify the seafloor bed deformation after a comparison with new bathymetric surveys.

In order to study the tsunami a 1/400 physical model, that closely followed the original bathymetry, was constructed at the Central Research Institute for Electric Power Industry (CRIEPI) in Abiko, Japan. The wave tank was 205m-long, 6m deep, and 3.5m-wide. A section of the physical model is presented in Figure 3.54 and its bathymetry is represented in Figure 3.55

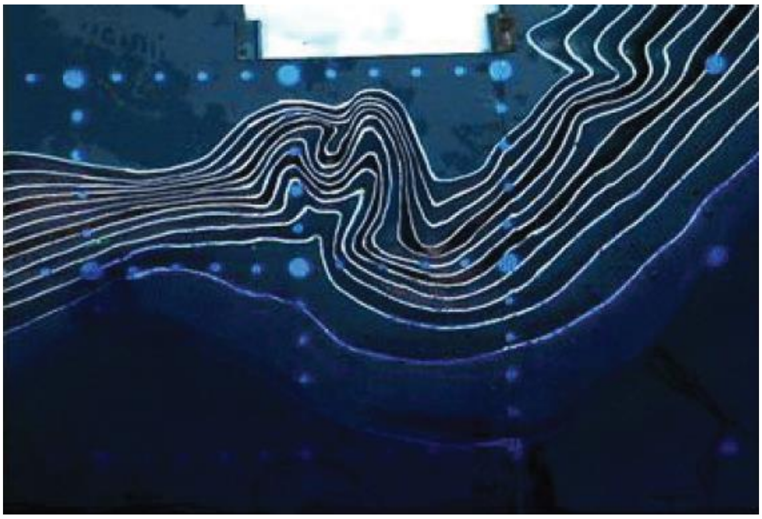

Figure 3.54 - Bathymetric profile for experimental setup for Monai Valley experiment. Taken from Synolakis et al. (2007).

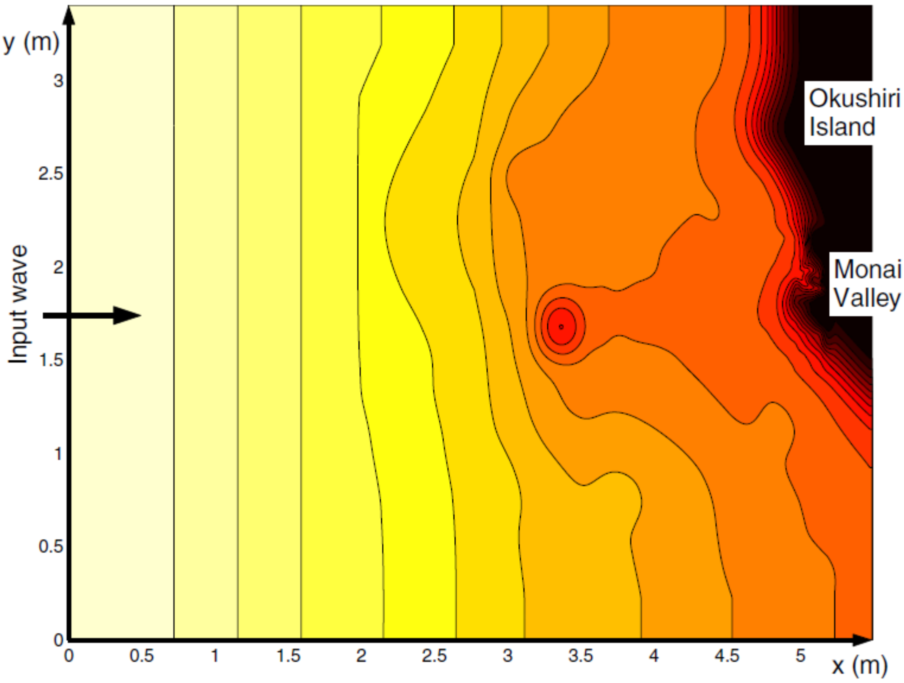

Figure 3.55 - Computational area for Monai Valley experiment. Taken from (Synolakis *et al.* 2007). No legend is provided.

The bathymetry used in the numerical simulations was scaled by a factor of 100:1 in relation to the physical model. The spatial resolution recommended by Synolakis et al. (2007) was followed with a spatial step in the x and y directions of 1.4 m.

The wave imposed in the experiments was an N wave (a type of solitary wave characterized by a trough followed by a crest) with a leading depression height of 2.5 cm and a crest of 1.6 cm. A profile of the imposed wave is presented in Figure 3.56. In the numerical model this wave was introduced as a time series in the boundary of the numerical grid.

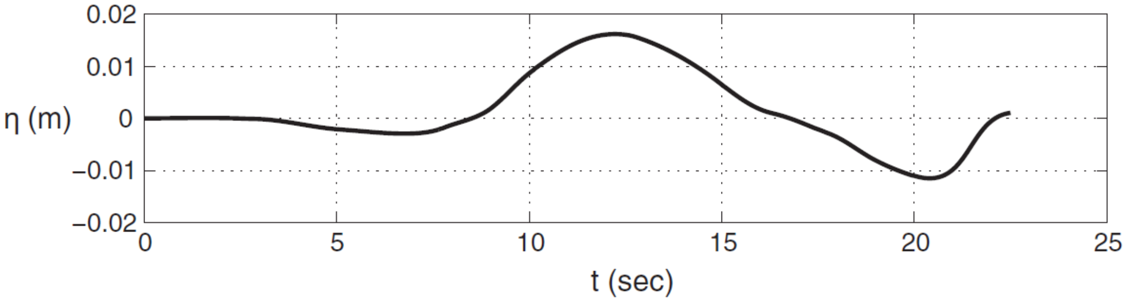

Figure 3.56 - Initial wave profile for Monai Valley experiment. Taken from Synolakis et al. (2007).

Time series of the water surface elevations observed during the experiments were recorded by 3 wave gauges, identified as p5, p7 and p9 in Figure 3.57 and positioned at the following coordinates, respectively: (x, y) = (4.521, 1.196), (4.521, 1.696), and (4.521, 2.196) in meters. The data recorded by the wave gauges and the comparison with the computed results is presented from Figure 3.58 to Figure 3.60.

Additionally, a video of the experiment can be found in NOAA’s centre for tsunami research website. A screenshot of this video, displaying the maximum run-up value observed in that particular trial, is compared to the maximum run-up values obtained for the numerical models’ simulations in Figure 3.61.

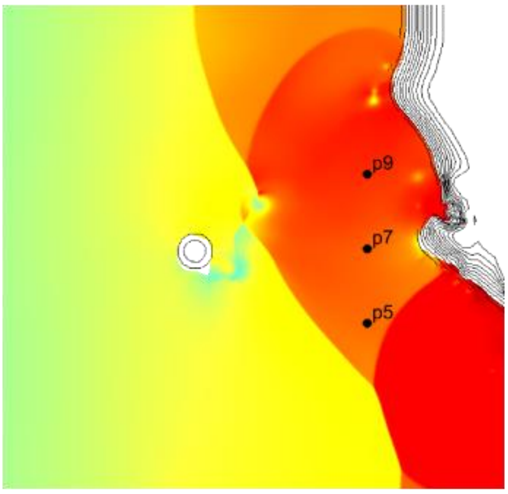

Figure 3.57 – Location of the wave gauges in the Monai Valley wave tank. Taken from Popinet (2016).

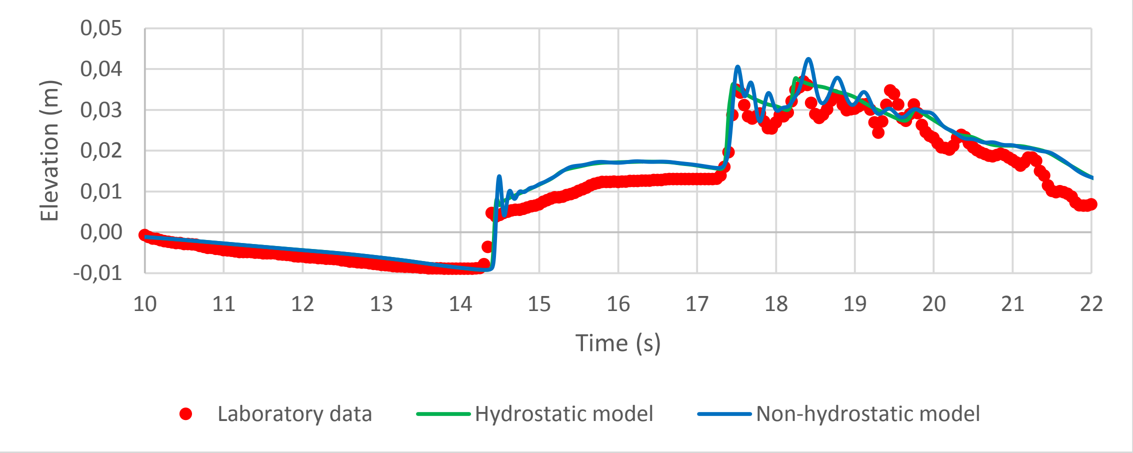

Figure 3.58 - Comparison between computed and measured time series for the Monai Valley wave tank. Gauge p9. Spatial step=1.4 m. Time step=0.01 s.

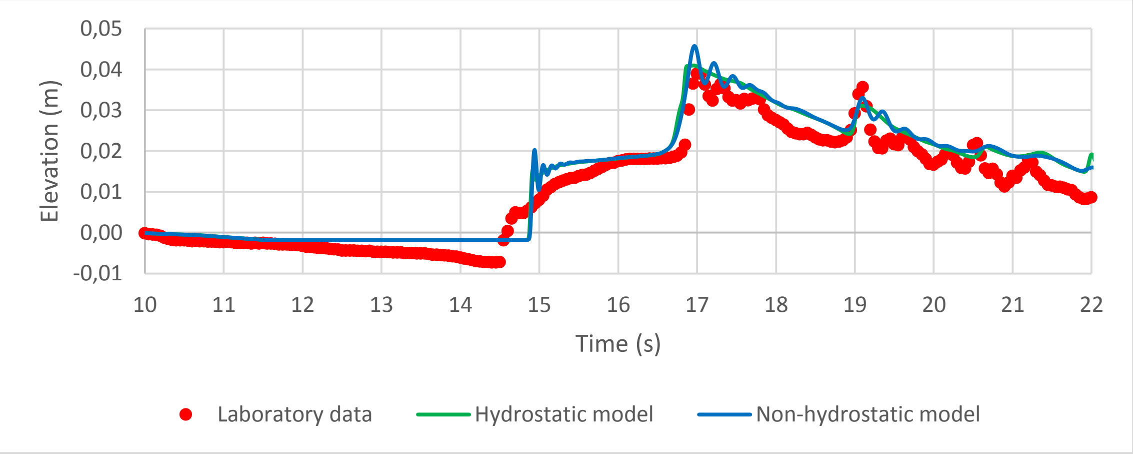

Figure 3.59 - Comparison between computed and measured time series for the Monai Valley wave tank. Gauge p7. Spatial step=1.4 m. Time step=0.01 s.

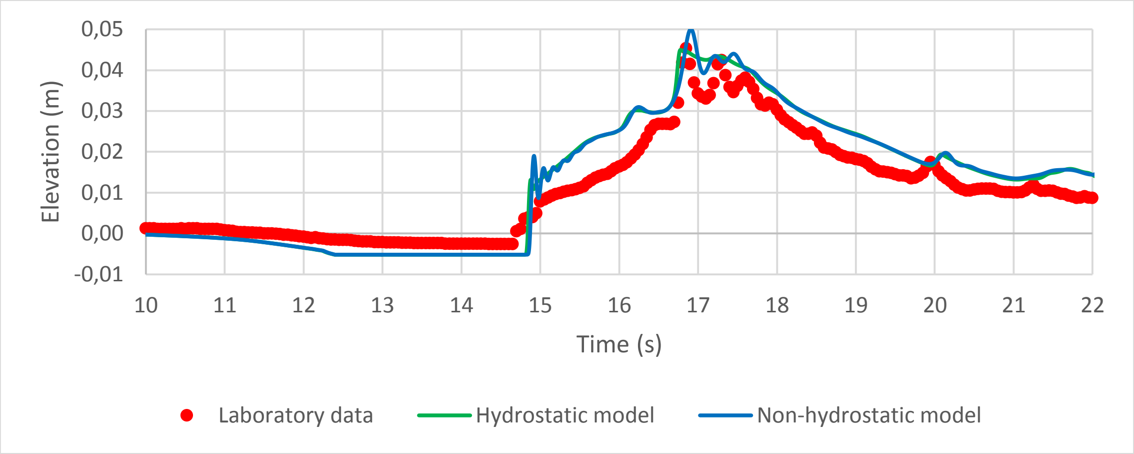

Figure 3.60 - Comparison between computed and measured time series for the Monai Valley wave tank. Gauge p5. Spatial step=1.4 m. Time step=0.01 s.

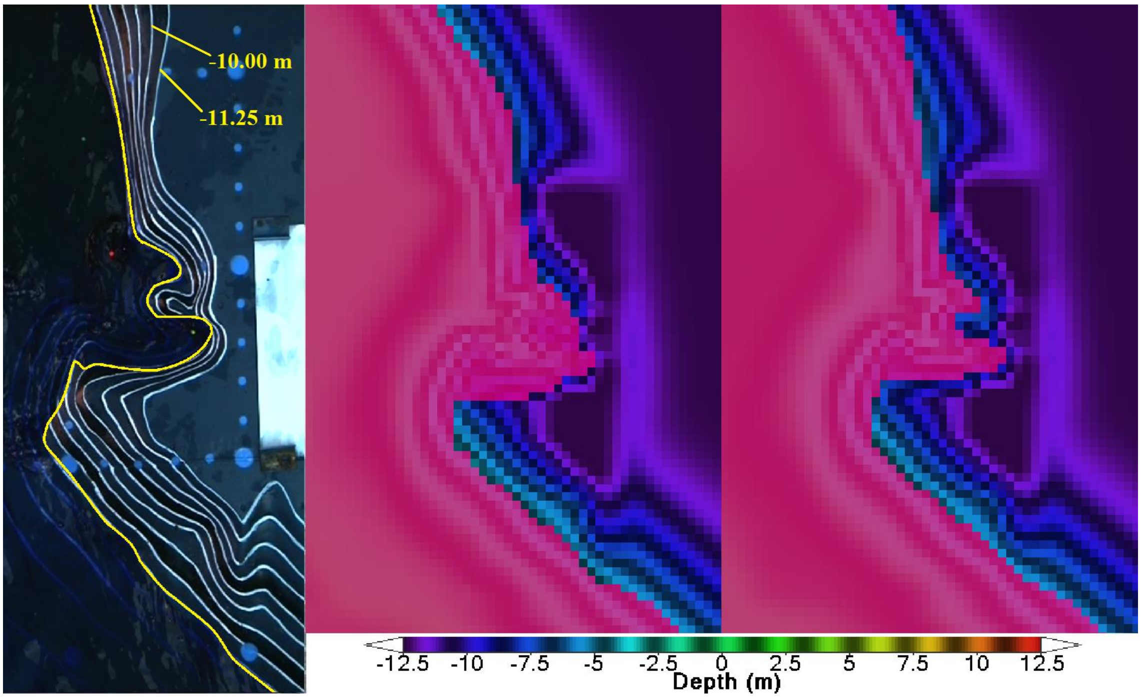

Figure 3.61 – Comparison of a screenshot from the video of the Monai Valley experiment (left), representing the maximum observed run-up, with the maximum run-up-values obtained from the non-hydrostatic model (centre) and the hydrostatic model (right).

As it can be observed in the time series graphics, both numerical models generate results in a good agreement with the measured data, with the hydrostatic model’s result actually having the best agreement with the maximum observed values. On the other hand, and since the hydrostatic model gives a much smoother solution the non-hydrostatic model is more accurate at simulating the several peaks observed in the profile recorded in the experiment’s time series. In relation to the phase, both models display equally good results.

In the video of the experiment a maximum run-up value of approximately 10 m is observed (in relation to the initial water level). When compared to the numerical models, the non-hydrostatic model produces the more accurate result with a simulated maximum run-up of 10.15 m against the 8.17 m simulated by the hydrostatic model. It should be noted in Figure 3.61 that the different outline of the wave front between the video's screenshot and the non-hydrostatic model can be explained by the fact that the first displays a single frame of the total experiment while the second shows all of the inundated cells in the full course of the test.

3.3. FIELD BENCHMARKING

Field benchmarking is an important step in the validation of a numerical model since the analytical or laboratory benchmarking tests, usually executed in controlled environments with precise input data, fail to fully guarantee a model's robustness in real world use. In the latter bathymetry is often more complex and there is lesser control over parameters such as initial and boundary conditions (Synolakis *et al.* 2007).

An example of the aforementioned problems is the generation of the tsunami wave form from measurable data, like the energy released by the earthquake. This can be done, for example, using a displacement model based on the works of Mansinha & Smylie (1971) or Okada (1985), but the obtained initial solution is unlikely to exactly match the real tsunami event.

On the other hand, field benchmarking doesn't suffer from the similarity problems mentioned in previous chapters, caused by the scales at which laboratory tests are performed.

In short, the comparison of the results produced by a numerical model with real-world data is a final important step for validating a model as apt for operational use.

3.3.1. TOHOKU EARTHQUAKE AND TSUNAMI

The Tohoku earthquake, or Great East Japan earthquake, was a magnitude 9.0 megathrust earthquake off the coast of Tohoku, Japan that occurred on 11 March 2011. The epicentre was located 70 km east of the Oshika Peninsula of Tohoku with a hypocentre at an underwater depth of approximately 30 km. This earthquake was the largest ever recorded in Japan and the fourth worldwide (Wikipedia, 2016).

This event triggered a devastating tsunami which propagated more than 5 km inland on the Sendai Plain, with its waves reaching heights of up to 39.7 m. This tsunami left a terrible aftermath of ten thousand casualties and damage costs of 309 billion US Dollars (Hyun *et al.* 2013).

This tsunami event was modelled using the hydrostatic version of MOHID by researchers at KORDI (Korean Ocean Research and Development Institute) with the objective of studying its propagation and inundation as well as to examine MOHID's applicability for this type of simulations.

In order to replicate the results of the aforementioned study, using both the hydrostatic and non-hydrostatic model, a request was made to KORDI, that was subsequently granted, for the supply of tidal gauge data, fault parameters for generation of the initial water level condition and bathymetry used in the Tohoku tsunami simulations.

The simulation conditions mirrored the ones presented in Hyun *et al.* (2013), which should be consulted for more detailed information, and will be briefly presented below.

The simulations were done on a 3 level nesting grid shown in Figure 3.62.

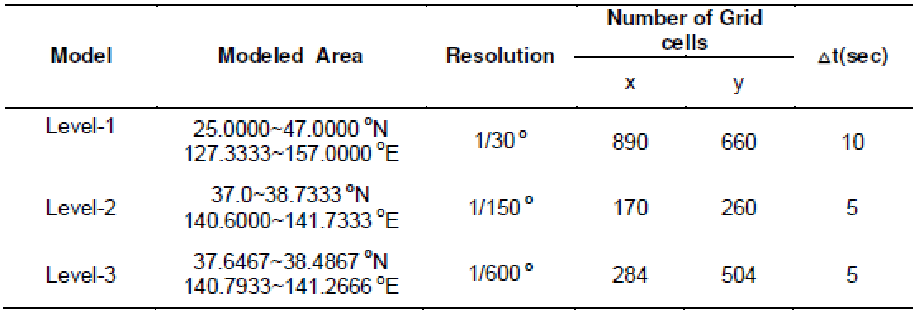

Model	Modeled Area	Resolution	Number of Grid cells		∆t(sec)
			x	y	
Level-1	25.0000~47.0000 °N 127.3333~157.0000 °E	1/30 °	890	660	10
Level-2	37.0~38.7333 °N 140.6000~141.7333 °E	1/150 °	170	260	5
Level-3	37.6467~38.4867 °N 140.7933~141.2666 °E	1/600 °	284	504	5

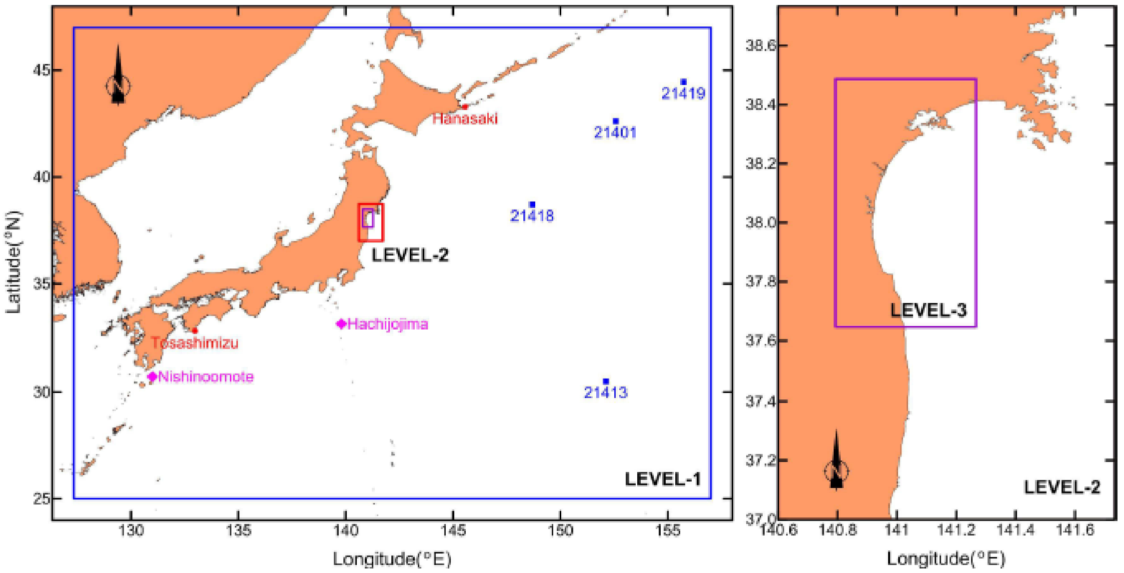

Figure 3.62 – Characteristics of the simulation domain with a three-level nesting grid system including observation stations: DART buoy (blue squares), IOC (red circles), and JCG (pink diamonds). Taken from Hyun *et al.* (2013)

The initial water displacement caused by the earthquake was calculated using the tsunami modelling package COMCOT (v1. 7) which follows the fault plane model proposed by Okada (1985). The fault parameters are presented in Figure 3.63.

	Lat. (°)	Lon. (°)	Depth (Fault Top, km)	Length (km)	Width (km)	Strike (°)	Dip (°)	Rake (°)	Slip (m)	M_w
Fault 1	38.80	144.00	5.1	186	129	203	16	101	24.7	8.8
Fault 2	37.33	142.80	17.0	194	88	203	15	83	6.1	8.3

Figure 3.63 – Fault parameters for the 2011 Tohoku earthquake. Taken from (Hyun *et al.* 2013).

For the Level-1 computational grid the simulation results obtained for both numerical models were compared with data recorded by NOAA's DART (Deep-ocean Assessment and Reporting of Tsunamis) buoys, UNESCO/IOC seal level station monitoring facility and Japan Coast Guard (JCG). These comparisons are presented from Figure 3.64 to Figure 3.71.

For the Level-3 computational grid the inundation maps generated from the numerical models' results were overlapped with radar satellite images displaying the observable inundation areas. These satellite images were taken by the RADARSAT satellite at 5:38 on March 13. In the images the inundation area can be identified by how radar reflects differently on different surfaces with inundated areas appearing dark and buildings looking very bright (Kokusai Kogyo Co., Ltd., 2011). The comparison between simulated and observable inundated areas is presented in Figure 3.72.

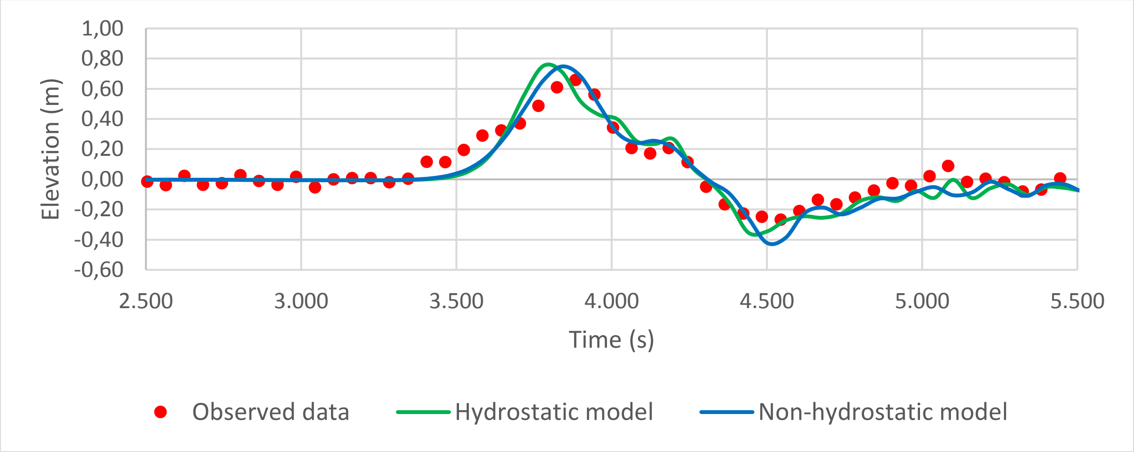

Figure 3.64 - Comparison between computed and measured time series for the Tohoku tsunami. Observed data obtained from DART buoy 21401.

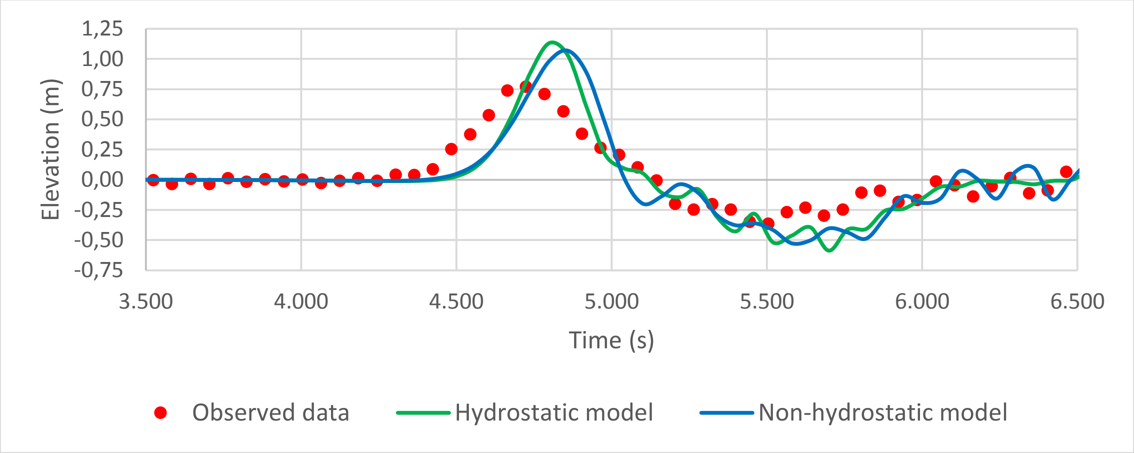

Figure 3.65 - Comparison between computed and measured time series for the Tohoku tsunami. Observed data obtained from DART buoy 21413.

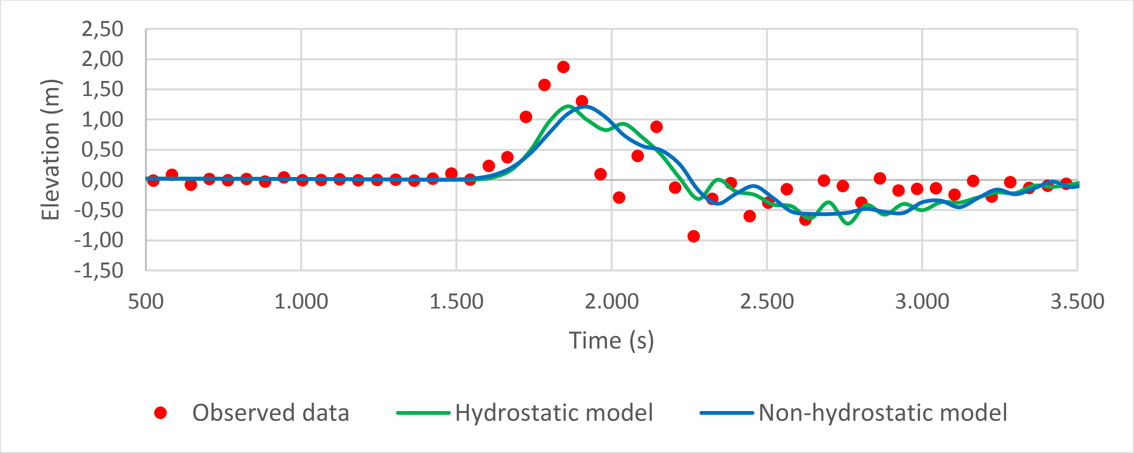

Figure 3.66 - Comparison between computed and measured time series for the Tohoku tsunami. Observed data obtained from DART buoy 21418.

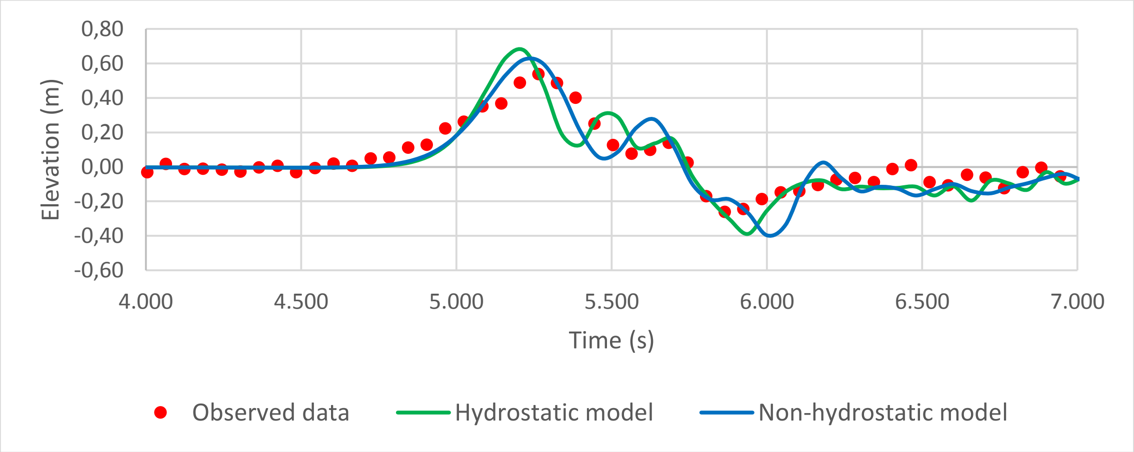

Figure 3.67 - Comparison between computed and measured time series for the Tohoku tsunami. Observed data obtained from DART buoy 21419.

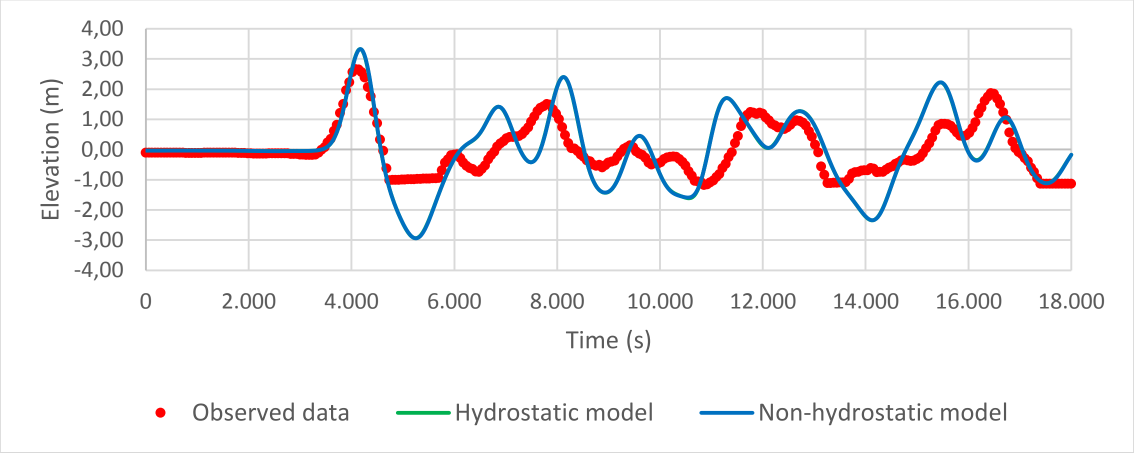

Figure 3.68 - Comparison between computed and measured time series for the Tohoku tsunami. Observed data obtained from IOC station for Hanasaki.

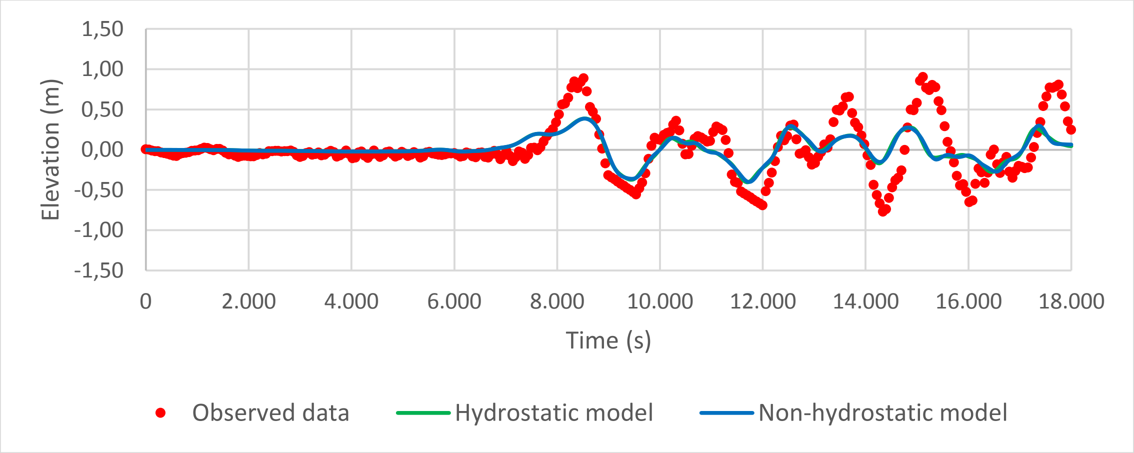

Figure 3.69 - Comparison between computed and measured time series for the Tohoku tsunami. Observed data obtained from IOC station for Tosashimizu.

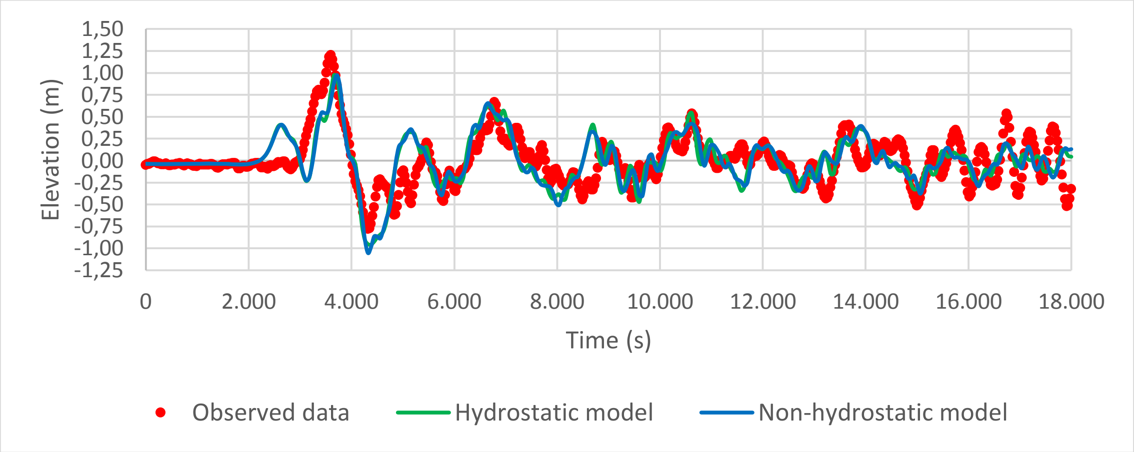

Figure 3.70 - Comparison between computed and measured time series for the Tohoku tsunami. Observed data obtained from the JCG for Hachijojima.

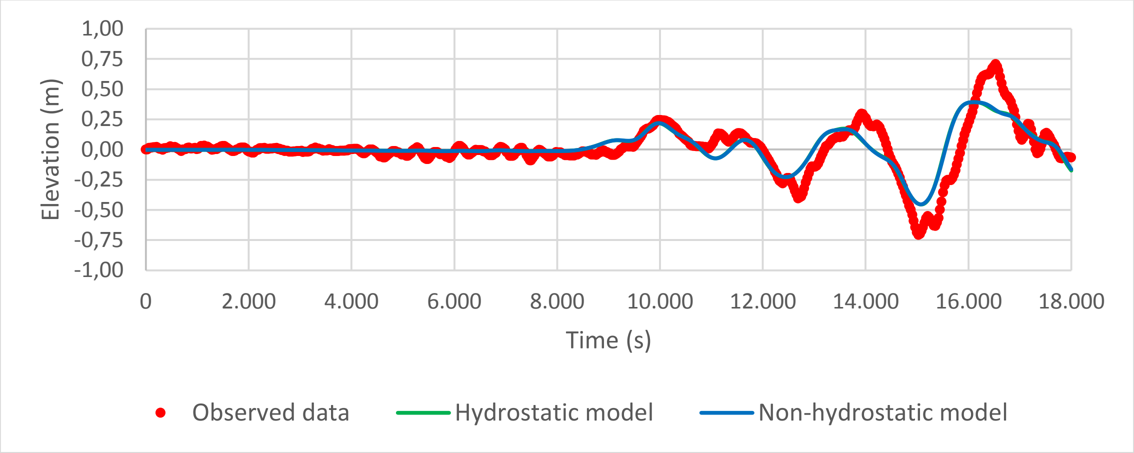

Figure 3.71 - Comparison between computed and measured time series for the Tohoku tsunami. Observed data obtained from the JCG for Nishinoomote.

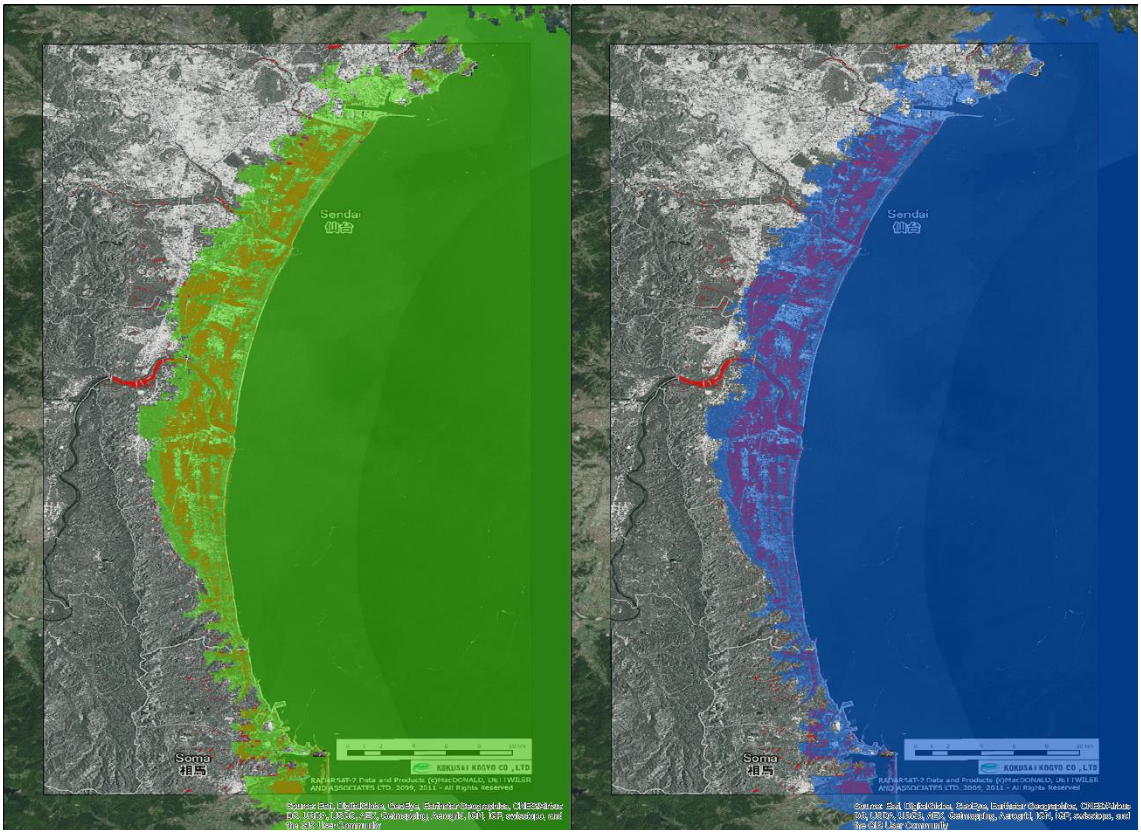

Figure 3.72 – Comparison of the observable inundated areas (red dots) with the inundation maps generated from the non-hydrostatic (left) and hydrostatic (right) models, for the Tohoku tsunami. The observable inundated areas were edited from RADARSAT satellite images by Kokusai Kogyo Co., Ltd. (Kokusai Kogyo Co., Ltd., 2011).

For the time series generated at the offshore stations, namely the DART buoys, there is a reasonable agreement between observed and computed results, with the non-hydrostatic model having a slight edge over the hydrostatic model.

Looking at the remaining stations, the non-hydrostatic and hydrostatic model’s results are virtually the same. For these stations, there is a reasonably good agreement between observed and computed data for Nishinoomote and Hachijojima while at the coastal stations of Tosashimizu and Hanasaki less ideal results are obtained.

The poor performance at Tosashimizu and Hanasaki coastal stations can be partially explained by the low resolution of the computational grid in an area where bathymetry may have a large influence over wave propagation and deformation induced by depth change. At the coastal stations locations the geometry and topography have a lesser influence in the tsunami propagation, thus better results are obtained (Hyun *et al.* 2013).

For the inundation maps, the observable and computed results seem to be fairly well matched, with inundation areas being mainly overestimated by the numerical models in the sections that presented bigger disparities. The agreement between observable and computed data could be potentially improved by using a higher resolution numerical grid with topography that contemplated the pre-exiting structures, such as buildings and sea walls.

4. CONCLUSIONS AND RECCOMENDATIONS

The main objectives of this dissertation were the validation of the non-hydrostatic version of MOHID, based on the pressure correction method presented in Cui *et al* (2012), and the comparison of the results with the ones produced by its hydrostatic counterpart. This way the benefits of using a non-hydrostatic model for the simulation of tsunamis could be assessed.

From the results presented in this dissertation it can be concluded that the non-hydrostatic model appears to be ready for use in tsunami propagation modelling due to the overall good fitting obtained for all the proposed test cases, including the ones that more closely represented real tsunami events.

In relation to its performance when compared to the hydrostatic version of MOHID, the non-hydrostatic model displayed much better results in the tests where the vertical acceleration component was more relevant, as it should be expected, in particular the test cases for the higher values of relative amplitudes. In the experiments that were more similar to real tsunami events the difference between models was less significant, with reasonably equivalent results for the wave propagation data. This can be explained by the fact that tsunami waves' propagation in the open sea can be approximated by the shallow water equations, which assume a small vertical velocity of the fluid (nearly hydrostatic). However, looking at the simple beach, conical island and Monai Valley experiments it appears that even for test cases that originated similar propagation results for both models, the non-hydrostatic model was consistently better at estimating the maximum run-up values. This is particularly relevant since the run-up is an important factor in the planning of mitigation measures against tsunami events.

This initial set of tests also shows great potential in the applicability of the model for the study of wind waves in complex geometries, such as ports, which is a feature that the current hydrostatic version of MOHID isn't able to perform. As such, this should be the focus of future studies involving the non-hydrostatic MOHID.

When it comes to possible improvements for the model, as it was demonstrated in the simple beach test case, the breaking wave module could be improved to better represent the complexity of the phenomenon.

REFERENCES

Archambeau, F., Guimet, V., & Bastin, G. (1999). *Application du prototype de module ALE du Solveur Commun à des cas de surface libre EDF HE-41/99/054/A.* Chatou, France: EDF Research and Development.

Baptista, M. A., Miranda, J. M., Lima, V., Catalão, J., & Roquette, P. (2008). *Avaliação do risco de tsunami na costa do Algarve.* Instituto de Ciências da Terra e do Espaço; Centro de Geofísica da Universidade de Lisboa; Instituto Dom Luiz.

Briggs, M. J., Synolakis, C. E., Harkins, G. S., & Green, D. R. (1995). Laboratory experiments of tsunami runup on a circular island. *Pure and Applied Geophysics, 144, 3/4*, 569-593.

Casulli, V., & Stelling, G. S. (1998). Numerical simulation of 3d quasi-hydrostatic, free-surface flows. *Journal of Hydraulic Engineering, 124*, 678-686.

Casulli, V., & Zanolli, P. (2002). Semi-implicit numerical modelling of non-hydrostatic free-surface flows for environmental problems. *Mathematical and Computer Modelling, 36*, 1131-1149.

Chen, C.-J., & Jaw, S.-Y. (1998). *Fundamentals of Turbulence Modeling.* Washington, D.C.: Taylor & Francis.

Chen, Q., Kirby, J. T., Dalrymple, R. A., Kennedy, A. B., & Chawla, A. (2000). Boussinesq modelling of wave tranformation, breaking and runup. II: 2D. *Journal of Waterway, Port, Coastal, and Ocean Engineering, 126*, 48-56.

Chen, Y.-Y., Li, M.-S., Hsu, H.-C., & Ng, C.-O. (2012). Theoretical and experimental study of particle trajectories for nonlinear water waves propagating on a sloping bottom. *Philosofical Transactions of the Royal Society A, 370*, 1543-1571.

Chorin, A. J. (1968). Numerical solution of the Navier-Stokes equations. *Mathematics of Computation, 22*, 745-762.

Cui, H., Pietrzak, J. D., & Stelling, G. S. (2012). Improved efficiency of a non-hydrostatic, unstructured grid, finite volume model. *Ocean Modelling, 54*, 55-67.

Fernandes, M. (2009). *Systematic comparison on the inundation response of AnuGA and COMCOT Tsunami modelling codes applied to the Boca do Rio and Alvor Bay area.* Faro: Faculdade de Ciências do Mar e do Ambiente da Universidade do Algarve.

Gardi, A., Valencia, N., Guillande, R., & André, C. (2011). Inventory of uncertainties associated with the process of tsunami damage assessment on buildings (SCHEMA FP6 EC co-funded project). *Natural Hazards and Earth System Sciences, 11*, 883-893.

Horrillo, J., Kowalik, Z., & Shigihara, Y. (2006). Wave dispersion study in the indian ocean - Tsunami of December 26, 2004. *Marine Geodesy, 29*, 149-166.

Hyun, S.-K., Choi, J.-Y., Lee, D.-Y., & Cho, K.-H. (2013). Tohoku eathquake, tsunami and innundation with MOHID. In M. Mateus, & R. Neves (Eds.), *Ocean modelling for coastal management – Case studies with MOHID* (pp. 131-141). Lisboa, Portugal: IST Press.

Keller, H. B. (1971). A new difference scheme for parabolic problems. In B. Hubbard (Ed.), *Numerical solutions of partial differential equations, Vol. II* (pp. 327-350). New York: Academic Press.

Kokusai Kogyo Co., Ltd. (2011, June 19). *Great East Japan Earthquake Archives Disaster on March 11, 2011 - Satellite images*. Retrieved from Japan Asia Group Kokusai Kogyo Co., Ltd.: http://www.kkc.co.jp/english/service/bousai/csr/disaster/201103_touhoku/aerial.html

Kulikov, E. (2006). Dispersion of the sumatra tsunami waves in the indian ocean detected by satellite altimetry. *Russian Journal of Earth Sciences, 8*, 1-5.

Leitão, P. C. (2016). *MOHID Hydrodinamic Module*. Retrieved from Github: https://github.com/Mohid-Water-Modelling-System/Mohid/blob/master/Software/MOHIDWater/ModuleHydrodynamic.F90

Liu, P. L.-F., Cho, Y.-S., Briggs, M. J., & Synolakis, C. E. (1995). Runup of solitary waves on a circular island. *Journal of Fluid Mechanics, 302*, 259-285.

Mansinha, L., & Smylie, D. E. (1971). The displacement fields of inclined faults. *Bulletin of the Seismological Society of America, 61*, 1433-1440.

Martins, F., Leitão, P., Silva, A., & Neves, R. (2001). 3D modelling in the Sado estuary using a new generic vertical discretization approach. *Oceanologica Acta, 24 (Suppl. 1)*, 51-62.

National Oceanic and Atmospheric Administration. (2015, December 17). *Physics of Tsunamis*. Retrieved from National Oceanic and Atmospheric Administration's Tsunami Warning Center: http://wcatwc.arh.noaa.gov/?page=tsunami_science

[NTHMP] National Tsunami Hazard Mitigation Program. (2012). *Proceedings and results of the 2011 NTHMP model benchmarking workshop.* Boulder: U.S. Department of Commerce/NOAA/NTHMP.

Okada, Y. (1985). Surface deformation due to shear and tensile faults in a half-space. *Bulletin of Seismological Society of America, 75*, 1135-1154.

Perot, J. B., & Subramanian , V. (2007). A Discrete Calculus Analysis of the Keller Box Scheme and a Generalization of the Method to Arbitrary Meshes. *Journal of Computational Physic, 226*, 494-508.

Popinet, S. (2016, January 14). *5.3 Tsunami runup onto a complex three-dimensional beach*. Retrieved from Gerris Flow Solver Sourceforge: http://gfs.sourceforge.net/examples/examples/monai.html

Shi, F., Kirby, J. T., & Tehranirad, B. (2012). *Tsunami benchmark results for spherical coordinate version of FUNWAVE-TVD.* Retrieved from University of Delaware: http://www.udel.edu/kirby/papers/shi-etal-cacr-12-02-version2.0.pdf

Silva, A. J. (1991). *Modelação matemática não linear de ondas de superfície e de correntes litorais* (Doctoral dissertation). Lisboa: Instituto Superior Técnico.

Smagorinsky, J. (1963). General circulation experiments with the primitive equations. I. The basic experiment. *Monthly Weather Review, 91*, 99-164.

Staroszczyk, R. (2011). Simulation of solitary wave mechanics by a corrected smoothed particle hydrodynamics method. *Archives of Hydro-Engineering and Environmental Mechanics, 58*, 23-45.

Stelling, G., & Zijlema, M. (2003). An accurate and efficient finite-difference algorithm for non-hydrostatic free-surface flow with application to wave propagation. *International Journal for Numerical Methods in Fluids, 43*, 1-23.

Synolakis, C. E. (1986). *The runup of long waves.* Pasadena, California: California Institute of Technology.

Synolakis, C. E. (1987). The runup of solitary waves. *Journal of Fluid Mechanics, 185*, 523-545.

Synolakis, C. E., & Bernard, E. N. (2006). Tsunami science before and beyond Boxing Day 2004. *Philosophical Transactions of the Royal Society A, 364*, 2231-2265.

Synolakis, C., Bernard, E., Titov, V., Kânoğlu, U., & González, F. (2007). *Standards, criteria, and procedures for NOAA evaluation of tsunami numerical models.* Seattle: NOAA/Pacific Marine Environmental Laboratory.

Theias, H. A. (2005). *Numerical Modeling of Non-Hydrostatic Processes in Estuarine and Coastal Regions* (Master's Thesis). Lisboa: Instituto Superior Técnico.

Tritton, D. J. (1977). *Physical Fluid Dynamics.* New York: Van Nostrand Reinhold Co.

US Army Corps of Engineers. (2016). *Tsunami Benchmark #2: Runup of Solitary Waves on a Circular Island*. Retrieved from US Army Corps of Engineers Coastal & Hydraulics Laboratory: http://chl.erdc.usace.army.mil/chl.aspx?p=s&a=Projects;35

US Army Corps of Engineers. (2016). *Tsunami Benchmark #3: Runup of Solitary Waves on a Vertical Wall*. Retrieved from US Army Corps of Engineers Coastal & Hydraulics Laboratory: http://chl.erdc.usace.army.mil/chl.aspx?p=s&a=Projects;36

Walters, R. A. (2005). A semi-implicit finite element model for non-hydrostatic (dispersive) surface waves. *Journal for numerical methods in fluids, 49*, 721-737.

White, F. M. (2005). *Viscous Fluid Flow.* New York: McGraw-Hill.

Wikipedia. (2016). *2011 Tōhoku earthquake and tsunami*. Retrieved from Wikipedia: https://en.wikipedia.org/wiki/2011_T%C5%8Dhoku_earthquake_and_tsunami